THE ATACAMA COSMOLOGY TELESCOPE: ACT-CL J0102−4915 "EL GORDO," A MASSIVE MERGING CLUSTER AT REDSHIFT 0.87

Felipe Menanteau[1], John P. Hughes[1], Cristóbal Sifón[2], Matt Hilton[3], Jorge González[2], Leopoldo Infante[2],
L. Felipe Barrientos[2], Andrew J. Baker[1], John R. Bond[4], Sudeep Das[5,6,7], Mark J. Devlin[8], Joanna Dunkley[9],
Amir Hajian[4], Adam D. Hincks[7], Arthur Kosowsky[10], Danica Marsden[8], Tobias A. Marriage[11], Kavilan Moodley[12],
Michael D. Niemack[13], Michael R. Nolta[4], Lyman A. Page[7], Erik D. Reese[8], Neelima Sehgal[14], Jon Sievers[4],
David N. Spergel[6], Suzanne T. Staggs[7], and Edward Wollack[15]

[1] Department of Physics & Astronomy, Rutgers University, 136 Frelinghuysen Rd, Piscataway, NJ 08854, USA
[2] Departamento de Astronomía y Astrofísica, Facultad de Física, Pontificía Universidad Católica de Chile, Casilla 306, Santiago 22, Chile
[3] School of Physics and Astronomy, University of Nottingham, University Park, Nottingham, NG7 2RD, UK
[4] Canadian Institute for Theoretical Astrophysics, University of Toronto, Toronto, ON M5S 3H8, Canada
[5] Berkeley Center for Cosmological Physics, LBL and Department of Physics, University of California, Berkeley, CA 94720, USA
[6] Department of Astrophysical Sciences, Peyton Hall, Princeton University, Princeton, NJ 08544, USA
[7] Joseph Henry Laboratories of Physics, Jadwin Hall, Princeton University, Princeton, NJ 08544, USA
[8] Department of Physics and Astronomy, University of Pennsylvania, 209 South 33rd Street, Philadelphia, PA 19104, USA
[9] Department of Astrophysics, Oxford University, Oxford, OX1 3RH, UK
[10] Physics & Astronomy Department, University of Pittsburgh, 100 Allen Hall, 3941 O'Hara Street, Pittsburgh, PA 15260, USA
[11] Department of Physics and Astronomy, The Johns Hopkins University, Baltimore, MD 21218-2686, USA
[12] Astrophysics & Cosmology Research Unit, School of Mathematical Sciences, University of KwaZulu-Natal, Durban 4041, South Africa
[13] NIST Quantum Devices Group, 325 Broadway Mailcode 817.03, Boulder, CO 80305, USA
[14] KIPAC, Stanford University, Stanford, CA 94305, USA
[15] Code 553/665, NASA/Goddard Space Flight Center, Greenbelt, MD 20771, USA

ABSTRACT

We present a detailed analysis from new multi-wavelength observations of the exceptional galaxy cluster ACT-CL J0102−4915, likely the most massive, hottest, most X-ray luminous and brightest Sunyaev–Zel'dovich (SZ) effect cluster known at redshifts greater than 0.6. The Atacama Cosmology Telescope (ACT) collaboration discovered ACT-CL J0102−4915 as the most significant SZ decrement in a sky survey area of 755 deg^2. Our Very Large Telescope (VLT)/FORS2 spectra of 89 member galaxies yield a cluster redshift, $z = 0.870$, and velocity dispersion, $\sigma_{\rm gal} = 1321 \pm 106$ km s^{-1}. Our *Chandra* observations reveal a hot and X-ray luminous system with an integrated temperature of $T_{\rm X} = 14.5 \pm 0.1$ keV and 0.5–2.0 keV band luminosity of $L_{\rm X} = (2.19 \pm 0.11) \times 10^{45} \, h_{70}^{-2}$ erg s^{-1}. We obtain several statistically consistent cluster mass estimates; using empirical mass scaling relations with velocity dispersion, X-ray $Y_{\rm X}$, and integrated SZ distortion, we estimate a cluster mass of $M_{200a} = (2.16 \pm 0.32) \times 10^{15} \, h_{70}^{-1} \, M_{\odot}$. We constrain the stellar content of the cluster to be less than 1% of the total mass, using *Spitzer* IRAC and optical imaging. The *Chandra* and VLT/FORS2 optical data also reveal that ACT-CL J0102−4915 is undergoing a major merger between components with a mass ratio of approximately 2 to 1. The X-ray data show significant temperature variations from a low of 6.6 ± 0.7 keV at the merging low-entropy, high-metallicity, cool core to a high of 22 ± 6 keV. We also see a wake in the X-ray surface brightness and deprojected gas density caused by the passage of one cluster through the other. Archival radio data at 843 MHz reveal diffuse radio emission that, if associated with the cluster, indicates the presence of an intense double radio relic, hosted by the highest redshift cluster yet. ACT-CL J0102−4915 is possibly a high-redshift analog of the famous Bullet cluster. Such a massive cluster at this redshift is rare, although consistent with the standard ΛCDM cosmology in the lower part of its allowed mass range. Massive, high-redshift mergers like ACT-CL J0102−4915 are unlikely to be reproduced in the current generation of numerical *N*-body cosmological simulations.

Key words: cosmic background radiation – cosmology: observations – galaxies: clusters: general – galaxies: clusters: individual (ACT-CL J0102−4915)

Online-only material: color figures

1. INTRODUCTION

There are currently only a few examples of merging cluster systems in which there are spatial offsets (on the order of 200–300 kpc) between the peaks of the total and baryonic matter distributions. Some of these, like 1E 0657−56 (the original "bullet" cluster at $z = 0.296$; Markevitch et al. 2002), A2146 (at $z = 0.234$; Russell et al. 2010), and possibly A2744 (at $z = 0.308$; Merten et al. 2011), contain in addition a cold, dense "bullet" of low-entropy gas that is clearly associated with the merger event. The offsets are due to the differing phys-

ical processes that act on the gas, galaxies, and dark matter. The gas behaves as a fluid, experiencing shocks, viscosity, and ram pressure, while the galaxies and dark matter (or so we posit) are collisionless. These bullet systems have been used to offer direct evidence for the existence of dark matter (Clowe et al. 2004, 2006) and to set constraints on the self-interaction cross section of the dark matter particle (Markevitch et al. 2004; Randall et al. 2008; Bradač et al. 2008). Additionally, the large merger velocity of 1E 0657−56 of around 3000 km s^{-1} (Mastropietro & Burkert 2008; Markevitch 2006), required to explain the morphology and temperature of the gas from

Chandra observations, is much higher than expected in cosmological simulations. These merging clusters provide interesting laboratories for several important topics in astrophysics and cosmology.

Merging cluster systems can display a wide range of mass ratios, impact parameters, types of merging systems, and times since closest approach, and clusters evolve with cosmic time. So it is worthwhile to find new bullet cluster systems, especially at high redshift, to exploit their different initial and final conditions and learn more about dark matter and the assembly of clusters through mergers. Massive clusters ($\sim 10^{15} M_\odot$) become increasingly rare at high z, while their infall speeds are typically higher in the early universe (see Lee & Komatsu 2010).

In this paper, we report on ACT-CL J0102−4915, a recently discovered system (Marriage et al. 2011) that appears to be an excellent new example of a bullet cluster at redshift $z = 0.87$. It was found by the Atacama Cosmology Telescope (ACT; Fowler et al. 2007) through its strong Sunyaev–Zel'dovich (SZ) signal (Sunyaev & Zeldovich 1972) and was confirmed through optical and X-ray data by Menanteau et al. (2010a). We demonstrate here that ACT-CL J0102−4915 is a rare and exceptional system at a time in cosmic history when the universe was only half its current age. Additionally, it is a contender for being the most massive and X-ray luminous galaxy cluster at $z > 0.6$, likely competitors being CL J1226+3332 (Maughan et al. 2004) at $z = 0.89$ with mass[16] of $M_{200c} = (1.38 \pm 0.20) \times 10^{15} h_{70}^{-1} M_\odot$ (Jee & Tyson 2009) and SPT-CL J2106−5844 at $z = 1.14$ with $M_{200a} = (1.27 \pm 0.21) \times 10^{15} h_{70}^{-1} M_\odot$ (Foley et al. 2011). Therefore, to reflect its exceptional mass and to recognize the Chilean contribution to ACT, we dub the cluster "El Gordo," which means "The Fat/Big One" in Spanish.

Throughout this paper, we quote cluster masses as M_{200a} (or M_{500c}), which corresponds to the mass enclosed within a radius where the overdensity is 200 (500) times the average (critical) matter density, and we assume a standard flat ΛCDM cosmology with $\Omega_m = 0.27$ and $\Omega_\Lambda = 0.73$ and give relevant quantities in terms of the Hubble parameter $H_0 = 70 h_{70}$ km s^{-1} Mpc^{-1}. For this cosmology the angular diameter distance to the cluster is $1617 h_{70}^{-1}$ Mpc and $1'$ corresponds to a physical scale of $470 h_{70}^{-1}$ kpc at the cluster redshift. Magnitudes are reported in the AB system and uncertainties are reported for 68% confidence intervals.

2. OBSERVATIONS

We have embarked on an ambitious multi-wavelength follow-up program aimed at characterizing the baryonic (i.e., gas, stellar) and dark matter mass components and the SZ–mass scaling relations of the most massive clusters discovered by ACT via the SZ effect. As part of this effort, we have obtained total mass estimates based on galaxy dynamics (via measuring spectroscopic redshifts with 8 m class telescopes; Sifón et al. 2012), cluster X-ray emission with *Chandra*, and stellar masses from infrared IRAC/*Spitzer* imaging. In the following sections, we describe the different data sets and preview the results when applied to this study of ACT-CL J0102−4915. Images of the cluster from these various data sources are shown in Figure 1.

2.1. SZ Observations

ACT is a 6 m off-axis telescope designed for arcminute-scale millimeter-wave observations and is situated at an elevation of 5190 m on Cerro Toco in the Atacama desert in northern Chile (see Fowler et al. 2010; Swetz et al. 2011 for a complete description). One of the goals of this project is to measure the evolution of structure in the universe using massive galaxy clusters detected via the SZ effect (e.g., Sehgal et al. 2011).

ACT observations began in late 2007, and to date it has surveyed two sky areas: one near declination −55° (the southern strip) and the other on the celestial equator. The 2008 southern observations covered a region of 455 deg², and recently ACT has analyzed an additional 300 deg² along the equator (centered on the SDSS Stripe82; Abazajian et al. 2009).

ACT-CL J0102−4915 was reported by ACT as a particularly strong SZ detection at a frequency of 148 GHz among 23 high-significance clusters from the 2008 southern survey (Marriage et al. 2011). In Figure 1 (lower right panel), we show the filtered ACT 148 GHz intensity maps for ACT-CL J0102−4915 using a matched filter (e.g., Haehnelt & Tegmark 1996; Melin et al. 2006).

The South Pole Telescope (SPT; Carlstrom et al. 2009) has reported its most significant cluster detections on a 2500 deg² survey (Williamson et al. 2011), which overlaps with the ACT 2008 southern survey. This sample also contains ACT-CL J0102−4915; it is SPT's most significant SZ cluster detection to date by nearly a factor of two, with a comparable beam-averaged SZ decrement to the Bullet cluster 1E 0657−56. Among all clusters in the combined ACT and SPT sample, ACT-CL J0102−4915 is exceptional in having the highest SZ signal (ACT; Marriage et al. 2011) or the highest significance SZ detection (SPT; Williamson et al. 2011).

2.2. Optical Imaging

The initial optical observations of ACT-CL J0102−4915 were carried out during 2009 December 9–12 using the SOI camera on the 4.1 m SOAR Telescope in Cerro Pachón (09B-0355, PI: Menanteau) using the Sloan Digital Sky Survey (SDSS) *griz* filter set with exposure times of 540 s (6 × 90 s), 720 s (6 × 120 s), 2200 s (8 × 275 s), and 2200 s (8 × 275 s) in *g*, *r*, *i*, and *z*, respectively. These exposure times were twice the nominal observations for the program as ACT-CL J0102−4915 was one of the targeted detections suspected to be a higher redshift cluster. The run conditions were optimal and all four nights were photometric with seeing in the range $0\rlap{.}''5$–$0\rlap{.}''9$. A complete description of the observations and data analysis is provided in Menanteau et al. (2010a).

As part of our 2010B spectroscopic follow-up campaign of the southern cluster sample, we secured additional deep and wider *Riz* imaging (intended for slit mask design) and extensive multi-object spectroscopy (MOS) with FORS2 on the Very Large Telescope (VLT; 086.A-0425 PI: Infante). FORS2 is a multi-mode (imaging, polarimetry, long slit, and MOS) optical instrument mounted on the UT1 (Antu) telescope. We devoted a total of 12 hr of observing time (service mode) on VLT to ACT-CL J0102−4915, of which 10 hr were devoted to MOS and 2 hr to imaging.

In our original confirmation of ACT-CL J0102−4915, we reported the larger concentration of galaxies to the NW as the optical cluster counterpart to the ACT source and used the brightest galaxy it contained as the cluster center (see Figure 1, top panels). However, even in the smaller $\approx 4\rlap{.}'5 \times 4\rlap{.}'5$ coverage

---

[16] Throughout this paper we distinguish between masses quoted with respect to the average or critical density using the "*a*" or "*c*" subscripts.
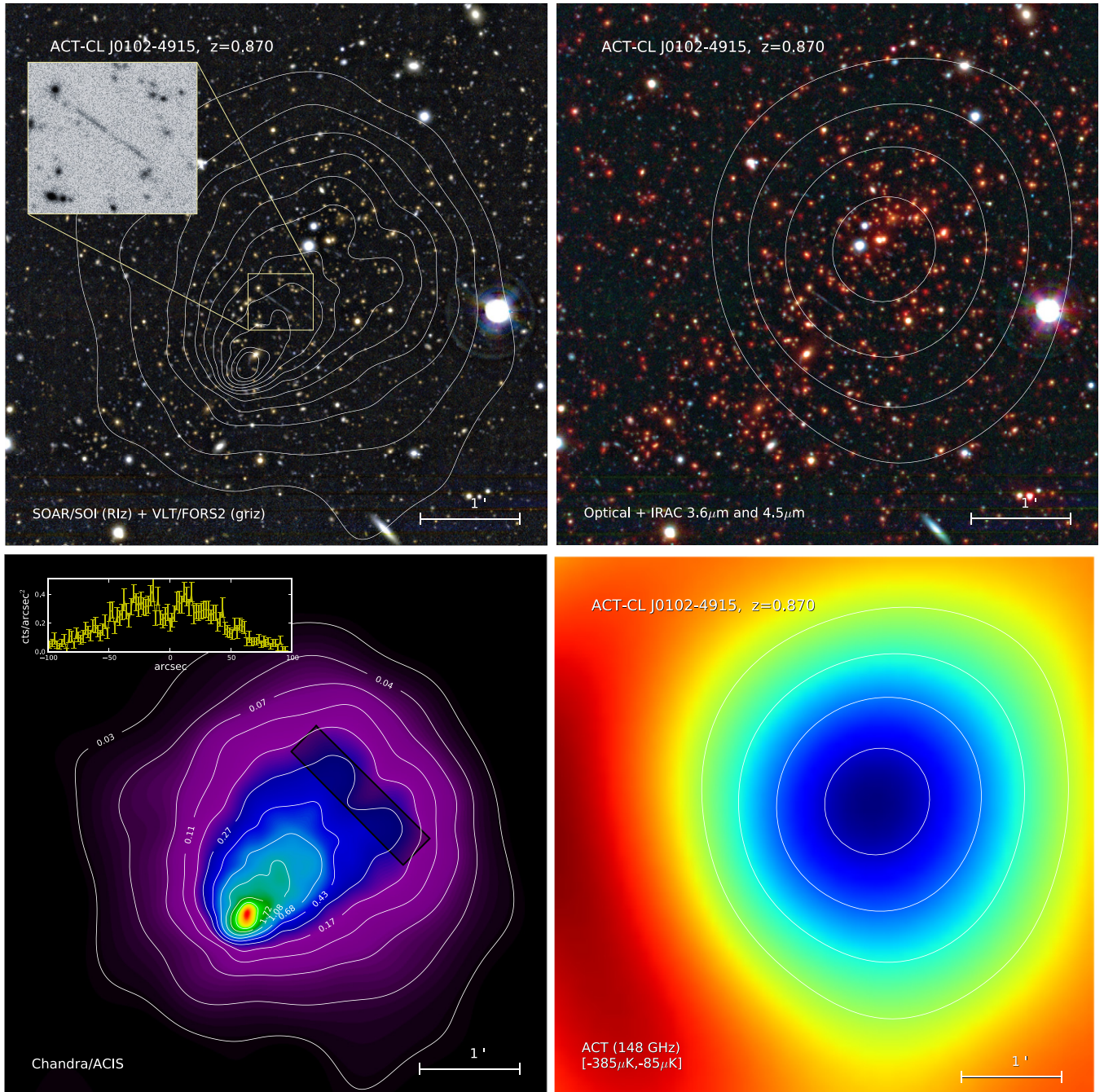
Figure 1. Multi-wavelength data set for ACT-CL J0102−4915 with all panels showing the same sky region. Upper left: the composite optical color image from the combined $griz$ (SOAR/SOI) and Riz (VLT/FORS2) imaging with the overplotted *Chandra* X-ray surface brightness contours shown in white. The black and white inset image shows a remarkably strong lensing arc. Upper right: the composite color image from the combination of the optical imaging from VLT and SOAR and IR from the *Spitzer*/IRAC 3.6 μm and 4.5 μm imaging. The overplotted linearly spaced contours in white correspond to the matched-filtered ACT 148 GHz intensity maps. Bottom left: false color image of the *Chandra* X-ray emission with the same set of 11 log-spaced contours between 2.71 counts arcsec^{-2} and 0.03 counts arcsec^{-2} as in the panel above. The inset here shows the X-ray surface brightness in a cut across the "wake" region from the box region shown. Bottom right: ACT 148 GHz intensity map with angular resolution of $1\!'.4$ and match-filtered with a nominal galaxy cluster profile, in units of effective temperature difference from the mean. The color scale ranges from -85 μK at the edges to -385 μK at the center of the SZ minimum. In all panels the horizontal bar shows the scale of the image, where north is up and east is left.

(A color version of this figure is available in the online journal.)

of the SOAR images (see Figure 9 from Menanteau et al. 2010a), we noted a number of red galaxies with similar photometric redshifts trailing toward the SE. The lack of coverage and large photometric redshift uncertainties made it difficult to confidently identify these galaxies as part of the cluster.

The FORS2/VLT imaging aimed to obtain wider and deeper observations to confirm the substructure hint in the SOAR data

and to secure galaxy positions for the spectroscopic observations. Our observations were carried out with the standard resolution of $0\!''.25$ pixel^{-1}, providing a field size of $6\!'.8 \times 6\!'.8$ with exposure times of 640 s (8×80 s), 2200 s (10×220 s), and 2300 s (20×115 s) in R, I, and z, respectively. The optical data were processed using a slightly modified version of the Python-based Rutgers Southern Cosmology image pipeline (Menanteau et al.

2009, 2010b) that takes us from raw data to galaxy catalogs. Here we give a brief overview of the steps involved and refer the reader to the above papers for a complete description. The initial standard CCD processing steps (i.e., flat fielding, bias subtraction) were performed via system calls to the ESO Recipe Execution tool (EsoRex).[17] In order to increase the depth and coverage for ACT-CL J0102−4915, we co-added the imaging in the r, i, and z and R, I, and z from SOAR and FORS2, respectively, into an *über* data set. As the FORS2 RIz images were taken under clear but non-photometric conditions, we utilize the SOAR photometric data to calibrate the photometry of the combined data. All science frames were aligned and median combined into a common pixel reference frame using SWarp (Bertin 2006) to a plate scale of $0{.}''2525$ pixel^{-1}. Source detection and photometry for the science catalogs were performed using SExtractor (Bertin & Arnouts 1996) in dual-image mode, in which sources were identified on the *über* i-band images using a 1.5σ detection threshold, while magnitudes were extracted at matching locations from all other bands.

2.3. Optical Spectroscopy and Redshifts

Based on the possibility that ACT-CL J0102−4915 was exceptional, we devoted the bulk (10 of 15 hr) of the awarded time on VLT in semester 2010B to securing spectra for galaxies with colors consistent with being early-type cluster members. We refer the reader to a companion paper (Sifón et al. 2012), where we fully describe the spectroscopic observing campaign of the 19 clusters at $z > 0.3$ in the ACT southern sample (of which ACT-CL J0102−4915 was part), including the data reduction, analysis, and redshift determination. Here we summarize the most salient aspects of this work.

The observations were executed in 2011 January under photometric conditions with seeing of $\lesssim 0{.}''8$. The observations cover the wavelength range ∼4000–8000 Å using the GRIS 300+11 Grism at 1.62 Å pixel^{-1} and resolution $\lambda/\Delta\lambda \sim 660$ at the central wavelength. At the cluster redshift of $z = 0.87$, the [O II] $\lambda3727$ emission lines, the Ca II ($K - H$, 3950 Å) (which is the spectral signature of elliptical galaxies), plus other absorption lines such as the G band (4300 Å) as well as the 4000 Å break were located in the spectral range of the grism. These features facilitated the determination of galaxy redshifts, galaxy cluster membership, and the galaxy velocity dispersion of the cluster. Integration times were 40 minutes per mask in order to maximize the number of galaxies while obtaining the necessary signal-to-noise ratio in the relevant lines. We observed a total of five FORS2/MXU masks in this configuration, providing redshifts for a total of 123 objects, of which 89 were cluster members.

The redshifts were measured by cross-correlating the spectra with galaxy spectral templates of the SDSS Data Release 7 (Abazajian et al. 2009) using the RVSAO/XCSAO package for IRAF (Kurtz & Mink 1998). Most of these member galaxies are ellipticals with no emission lines, and only a few emission-line galaxies have been found to belong to the cluster.

Cluster membership was determined using a rest-frame cut in velocity space of $4000\,\mathrm{km\,s^{-1}}$ and then applying the shifting gapper method of Katgert et al. (1996) in order to remove galaxies that lie outside a given gap in velocity space from the main body of galaxies. In particular, we defined the main body in bins of 15 galaxies and used a velocity gap of $500\,\mathrm{km\,s^{-1}}$. We used the well-accepted biweight estimator (Beers et al.

velocity (km/s)

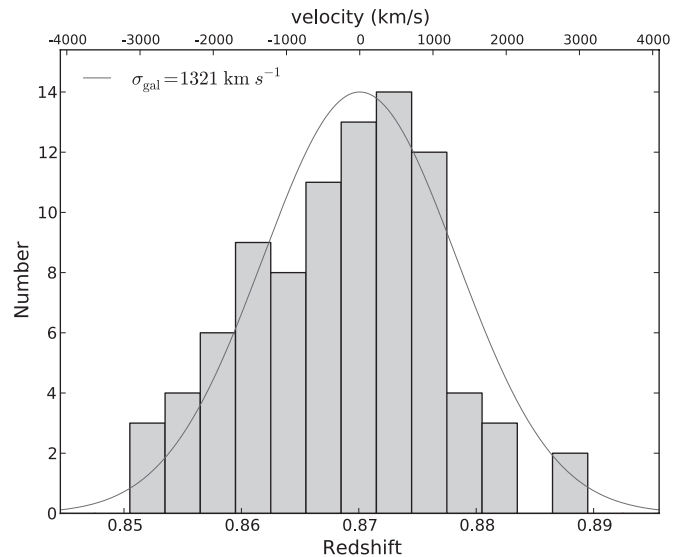**Figure 2.** Histogram showing the redshift distribution for the 89 cluster member galaxies and the Gaussian with the same mean and width σ_gal.

1990) to estimate both the mean redshift of the sample, $z = 0.87008 \pm 0.00010$, and the velocity dispersion[18] of the cluster, $\sigma_\mathrm{gal} = 1321 \pm 106\,\mathrm{km\,s^{-1}}$. Errors were estimated via bootstrap resampling. The velocity dispersion of ACT-CL J0102−4915 is larger than that of all other clusters in the ACT sample (Menanteau et al. 2010a; Sifón et al. 2012) and also larger than that of SPT-CL 2106−5844, which is the largest in the full 2500 deg^2 SPT sample (Foley et al. 2011; Williamson et al. 2011). Using only the passive galaxies (i.e., objects with no emission lines) in ACT-CL J0102−4915, we obtained a mean redshift of $z = 0.86963 \pm 0.00012$ with a velocity dispersion of $1280 \pm 108\,\mathrm{km\,s^{-1}}$.

In Figure 2, we show the redshift distribution for all galaxy members from the FORS2 spectra. We see no indication of substructure along the line of sight, confirming the conclusion of Sifón et al. (2012), which used the Dressler & Shectman (1988) test. However, as we will discuss in Section 3.2, we find substantial evidence for spatial substructure.

2.4. Chandra X-Ray Observations

We were awarded 60 ks of *Chandra* observing time on this target during cycle 12 (PI: Hughes, ObsID: 12258) as part of our follow-up effort on the SZ clusters found in the ACT 2008 455 deg^2 survey (Menanteau et al. 2010a). The *Chandra* observation was carried out on 2011 January 26 and 27 for an effective exposure of 59,260 s using the ACIS-I array. Figure 1 (bottom left panel) shows the surface brightness of the cluster after point-source removal, exposure correction, and adaptive kernel smoothing.

The cometary appearance of the X-rays is remarkable, extending even to the apparent presence of two "tails" extending off toward the NW. Orthogonal slices of the X-ray surface brightness show that these "tails" arise from significant depressions in the X-ray intensity, at a level of 20%–40%, in a band extending from about 1′ NW of the compact peak emission region and continuing off to the NW out to the faint parts of the cluster. The depression is about 35″ (270 h_{70}^{-1} kpc) wide. We refer to this feature as the "wake."

---

[17] http://www.eso.org/sci/software/cpl/esorex.html

[18] As customary, the quoted uncertainties for z and σ_gal only reflect statistical errors from 89 objects and do not include systematic effects.
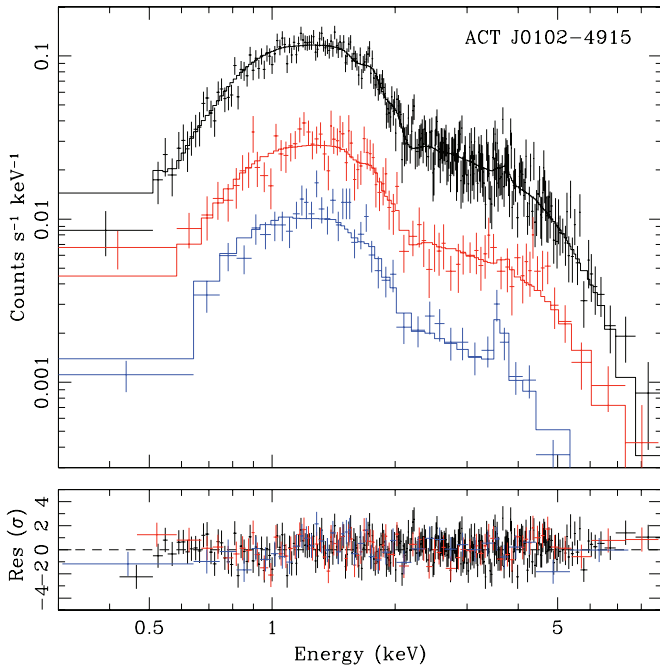
Figure 3. *Chandra* X-ray spectra of ACT-CL J0102−4915 for the total cluster in black, the cool bright peak (region 1 in Figure 5) in blue, and the highest temperature region (region 5) in red. The bottom panel shows the residuals between the best-fit models (histograms in top panel) and data.

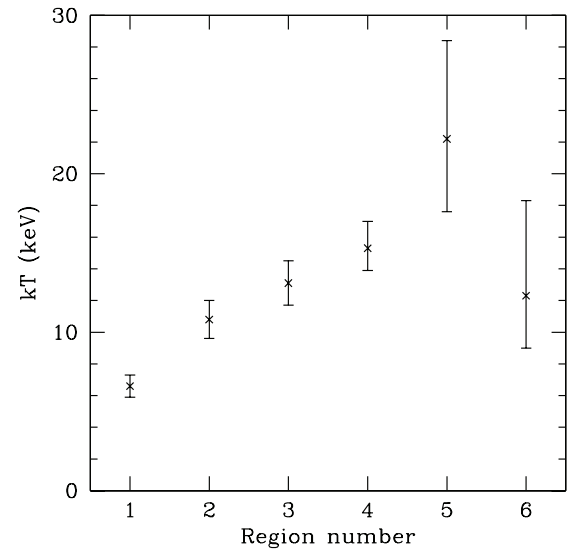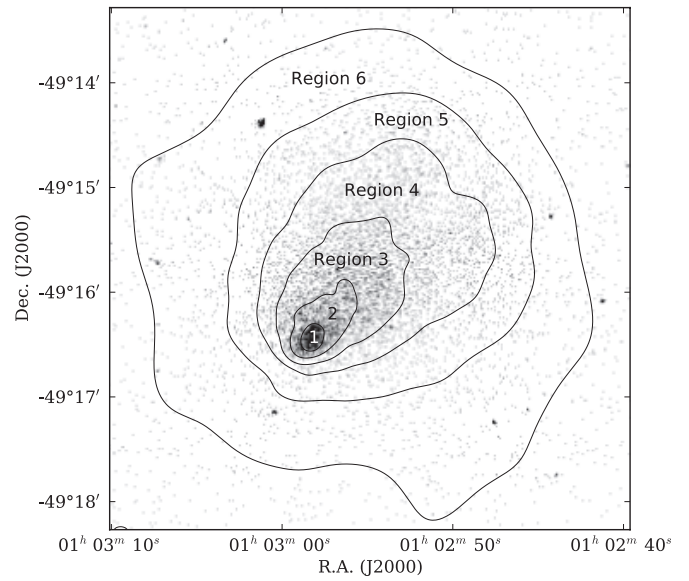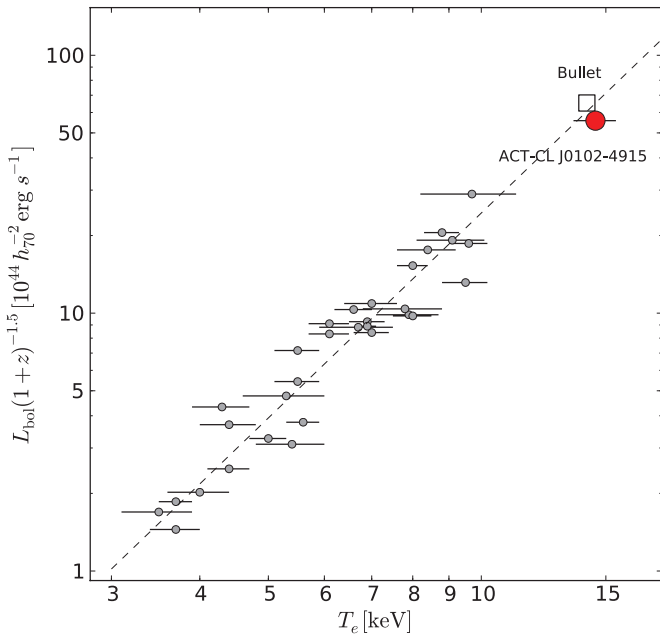(A color version of this figure is available in the online journal.)

Figure 4. X-ray bolometric luminosity vs. temperature for a sample of well-studied clusters taken from Markevitch (1998). The Bullet cluster (1E 0657−56) is the open square point at high temperature and luminosity from Markevitch (2006). ACT-CL J0102−4915 is the red circle in the same region of the plot.

(A color version of this figure is available in the online journal.)

The integrated *Chandra* spectrum is shown in Figure 3 (top black points). The extraction region for this spectrum excludes the central peak emission (from within the innermost contour in Figure 1) and extends out to the outermost contour in Figure 1, which is at a radius of around $2'.2$ ($1.0\,h_{70}^{-1}$ Mpc). An absorbed `phabs*mekal` model yielded a best-fit (source frame) temperature of $kT = 14.5 \pm 1.0$ keV, metal abundance

Figure 5. Upper panel: *Chandra* X-ray image showing raw detected counts and the spectral extraction regions. Lower panel: best-fitted X-ray temperatures plotted vs. spectral extraction region (see key in figure to left). Error bars are 1σ. Region 1, corresponding to the bright peak, is the coolest region.

0.19 ± 0.09 with respect to solar values, and a bolometric luminosity of $L_{bol} = 13.6 \times 10^{45}\,h_{70}^{-2}$ erg s^{-1}. Figure 4 shows the L_{bol}–T_X relation with ACT-CL J0102−4915 added as the red point (note that a redshift correction factor of $(1 + z)^{-1.5}$ was applied to L_{bol} following Vikhlinin et al. 2002). The nearby point on this figure is the closest comparison cluster, 1E 0657−56. Similarly, the X-ray luminosity of ACT-CL J0102−4915 in the 0.5–2.0 keV band is $L_X = 2.19 \pm 0.11 \times 10^{45}\,h_{70}^{-2}$ erg s^{-1}.

The modest count rate of ACT-CL J0102−4915 (i.e., 0.2 s^{-1} corresponding to a total number of detected X-ray photons of nearly 12,000) limits the number of regions into which the cluster can be subdivided for spatially resolved spectroscopy. We perform this measurement by dividing the total emission into roughly equal parts as shown in Figure 5. Spectra were extracted and fitted to the same absorbed thermal model as before; the best-fit temperatures are plotted versus region number in Figure 5. The coolest (region 1, $kT = 6.6 \pm 0.7$ keV) and the hottest (region 5, $kT = 22^{+6}_{-5}$ keV) spectra are plotted in Figure 3
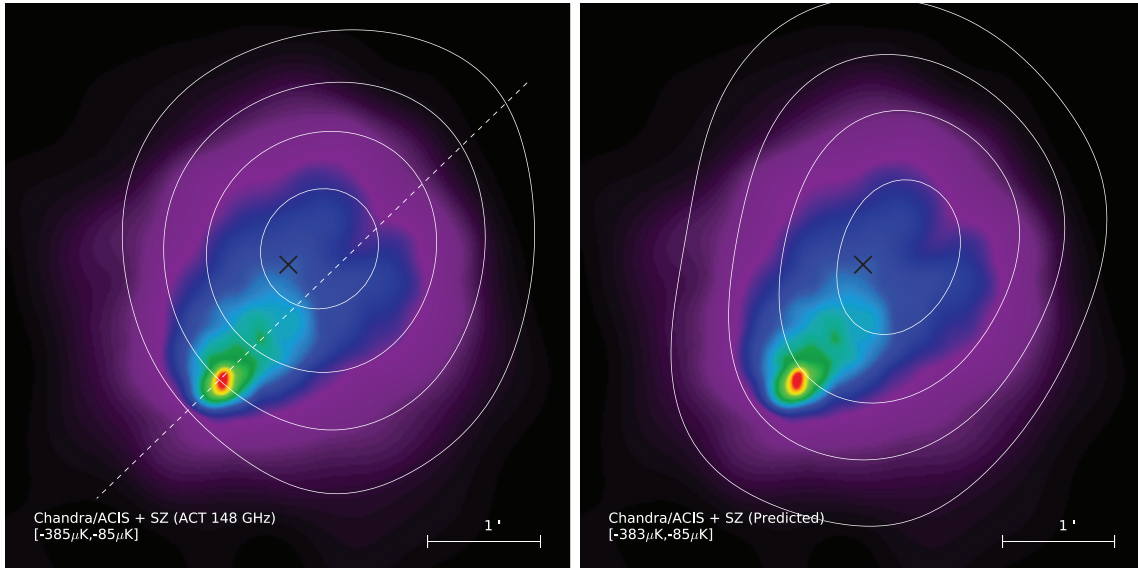
Figure 6. X-ray *Chandra* emission overlaid with the ACT 148 GHz data contours from Figure 1 (left) and the predicted SZ signal at 148 GHz from the deprojected X-ray data (right). The black cross represents the SZ position reported by Williamson et al. (2011) for ACT-CL J0102−4915. The contour levels are linearly spaced between the limits shown in brackets on each panel. The minimum central value of the ACT and predicted signals agree to within ∼15%. The white dotted line shows the symmetry axis chosen for the deconvolution.

(A color version of this figure is available in the online journal.)

in blue and red, respectively. Note the strong Fe K line (observed at $E = 3.56$ keV) in the spectrum of the coolest region, which yielded a rather high metal abundance of 0.57 ± 0.20. Elsewhere the Fe K line is not detected strongly, pointing to abundance variations in the cluster gas.

We see that the peak emission region in ACT-CL J0102−4915 is an X-ray-bright, relatively cool "bullet" of low-entropy gas like in 1E 0657−56. The enhanced Fe abundance suggests that it was the core of a cool-core cluster that has, so far, survived a high-velocity merger with another system. The cluster's high overall gas temperature and spatial temperature variations (Figure 3) argue for significant amounts of shock heating of the gas. The steep falloff in the X-ray surface brightness toward the SE, as well as the "wake" in the main cluster gas toward the NW, clearly indicates that the bullet is moving toward the SE.

The two lower panels of Figure 1 show that the SZ and X-ray peaks are displaced by about $1\farcm2$. Similar offsets between the peak SZ and X-ray emission have also been reported in the bullet-like cluster A2146 at $z = 0.23$, for which *Chandra* and Arcminute Microkelvin Imager (AMI) observations at 13.9–18.2 GHz show a remarkably similar separation of the SZ and X-ray signal distributions (see AMI Consortium: Rodríguez-Gonzálvez et al. 2011, their Figures 13 and 15). Two factors contribute to this. First, X-ray emission is more sensitive to denser parts of the cluster, since X-ray surface brightness is proportional to $\int n_e^2 T_e^\alpha dl$, where n_e and T_e are the electron number density and temperature and $\alpha \simeq 0.1$ (for band-limited X-ray emission at high temperature), while the SZ signal is proportional to the line-of-sight gas pressure $\int n_e T_e dl$. Second, the combination of *Chandra*'s and ACT's widely different angular resolutions ($<1''$ versus $1\farcm4$) is particularly relevant for observations of merging clusters with complex gas density substructure.

In order to investigate these differences, we developed a new technique for deprojecting X-ray images that, unlike traditional methods utilizing azimuthally averaged profiles, takes account of the full observed two-dimensional structure. The process assumes rotational symmetry about a user-defined axis and independently deprojects each column of pixels perpendicular

to that axis. For ACT-CL J0102−4915, we chose the symmetry axis so that it runs through both the peak X-ray emission at the bullet and the surface brightness depression toward the NW. The axis is centered on R.A. = 01:02:54.9, decl. = −49:15:52.5 and oriented at a position angle of 136° (see Figure 6). Beyond a certain radius from the center ($1\farcm65$ in the case of ACT-CL J0102−4915), where the surface brightness is background dominated, we used an analytic β-profile fit to the azimuthally averaged data to deproject the cluster emission smoothly to large radii. Interior to this radius, using the adaptively smoothed, 0.5–2.0 keV band image, we deproject the X-ray surface brightness in strips perpendicular to the symmetry axis. Deprojection of the cluster emission is done in the usual manner ("peeling the onion") using the best-fit integrated spectral parameters given above to relate the X-ray emission to the gas density of each deprojected shell. We deproject the north and south parts of the cluster separately but interpolate the density value across the cluster when "peeling" back any individual layer (to avoid a discontinuity at the symmetry axis). In general, this process is not guaranteed to produce positive definite values (as physically required), so we force the computed density to be zero in cases where the deprojection would result in a negative (or more precisely, imaginary) value. We quote electron density values using an electron-to-proton number ratio of $n_e/n_p = 1.2$, and for mass densities we assume a mean mass of $1.4 m_p$.

The deprojection results in an estimate of the three-dimensional distribution of the gas density in the cluster. From this we compute the predicted SZ signal at 148 GHz. Since the SZ depends linearly on the gas temperature, as a first approximation, we use the fitted X-ray temperatures in the six regions shown in Figure 3 to generate a temperature-corrected SZ map of the cluster. This was done by computing the ratio of expected SZ signal (Nozawa et al. 1998) for the observed temperatures in each of the six regions to the average cluster temperature and multiplying the single-temperature SZ map by the appropriate ratio for the region. The multiplicative ratios vary from a value of 0.5 (region 1) to 1.6 (region 5). A more refined calculation

would take into account the deprojection of the X-ray temperatures; however, for our purposes here (i.e., to study the centroid differences), the simpler approximation is sufficient.

This temperature-corrected SZ map is then convolved with the ACT beam model (Hincks et al. 2010), added to a source-free region of the ACT map in the vicinity ACT-CL J0102−4915 (to include similar cosmic microwave background (CMB) and instrumental noise), and then is filtered with the same procedure used to detect ACT-CL J0102−4915. In Figure 6, we show contours of the predicted SZ signal overlaid on the *Chandra* data (right), next to an identical plot with contours of the ACT data (left). The resulting centroid difference between the peak of the SZ signal and the simulated SZ map is 6″, which is within the expected positional error circle. Furthermore, the intensity of the predicted SZ signal agrees to within ∼15% with the ACT data. To conclude, we note that the offset between the peak X-ray and SZ signals is predominantly a result of the different sizes of the beams between *Chandra* and ACT (at least a factor of 60).

2.5. Spitzer/IRAC Imaging

As part of a larger warm-phase *Spitzer* program (PID: 70149, PI: Menanteau) that aims to characterize the stellar mass content of clusters in the ACT sample (M. Hilton et al. 2012, in preparation), in 2010 August we obtained IRAC 3.6 μm and 4.5 μm observations of ACT-CL J0102−4915. Our observations were designed to provide coverage out to the virial radius for clusters at $z > 0.4$, using a 2×2 grid of IRAC pointings centered on the cluster position. A total of 10×100 s frames were obtained in each channel at each grid position, using a large-scale cycling dither pattern. The basic calibrated data images were corrected for pulldown using the software of Ashby & Hora[19] and then mosaiced using MOPEX (Makovoz & Khan 2005) to give maps that are ≈ 13′ on a side with 0″.6 pixel scale. The maps for each channel were then registered to a common pixel coordinate system. By inserting synthetic point sources, we estimate the 80% completeness depths of the final maps to be ≈ 22.6 mag (AB) in both channels.

Matched aperture photometry was performed on the IRAC maps using SExtractor in dual-image mode, using the 3.6 μm channel as the detection band. We measure fluxes through 4″ diameter circular apertures, which are corrected to estimates of total magnitude using aperture corrections (as measured by Barmby et al. 2008) of −0.35 ± 0.04 and −0.37 ± 0.04 mag in the 3.6 μm and 4.5 μm channels, respectively. The photometric uncertainties were scaled upward by factors of 2.8 and 2.6 in the 3.6 μm and 4.5 μm channels, respectively, in order to account for noise correlation between pixels introduced in the production of the mosaics that is not taken into account in the SExtractor error estimates. These scaling factors were determined using the method outlined in Barmby et al. (2008). Finally, the uncertainties in the aperture corrections were added to the photometric errors in quadrature.

3. ANALYSIS AND RESULTS

3.1. Mass Estimation

Here we estimate the mass for ACT-CL J0102−4915 using all the mass proxies available from the X-ray data and optical spectroscopy. We present values in Table 2 and discuss them in

detail in the next sections. In all cases we quote uncertainties that include measurement errors as well as the uncertainties in scaling relations between observables and cluster mass relation. For the dynamical and X-ray masses, scaling to the common mass estimator M_{200a} carries additional uncertainty that we quantify below and include in the table.

3.1.1. Dynamical Mass

Here we report in more detail the dynamical mass estimates for ACT-CL J0102−4915 calculated by Sifón et al. (2012). The velocity dispersion of the cluster is $\sigma_{\mathrm{gal}} = 1321 \pm 106$ km s^{-1}. This matches the largest reported dispersion of all known clusters at $z > 0.6$ from RX J0152.7−1357 at $z = 0.836$ and $\sigma_{\mathrm{gal}} = 1322^{+74}_{-28}$ km s^{-1} (Girardi et al. 2005), although note that the quoted velocity dispersion is for a well-studied merging system that is resolved into two components of considerably lower mass. We use the M_{200c}–σ_{DM} scaling relation from Evrard et al. (2008) to convert the measured velocity dispersion into a dynamical mass estimate,

$$M_{200c} = \frac{10^{15}}{0.7 h_{70}(z)} \left(\frac{\sigma_{\mathrm{DM}}}{\sigma_{\mathrm{DM},15}} \right)^{1/\alpha} M_\odot, \qquad (1)$$

where $h_{70}(z) = h_{70}\sqrt{\Omega_m(1+z)^3 + \Omega_\Lambda}$, $\sigma_{\mathrm{DM},15} = 1082.9 \pm 4.0$ km s^{-1}, $\alpha = 0.3361 \pm 0.0026$, and σ_{DM} is the velocity dispersion of the dark matter halo. The latter is related to the observed galaxy velocity dispersion by the velocity bias parameter, $b_v = \sigma_{\mathrm{gal}}/\sigma_{\mathrm{DM}}$. The latest physically motivated simulations (see Evrard et al. 2008, and references therein) indicate that galaxies are essentially unbiased tracers of the dark matter potential, $\langle b_v \rangle = 1.00 \pm 0.05$. Using a bias factor of $b_v = 1$ for the velocity dispersion for all galaxies, we obtain a dynamical mass of $M_{200a,\mathrm{dyn}} = 1.86^{+0.54}_{-0.49} \times 10^{15} h_{70}^{-1} M_\odot$. Similarly, using only the passively evolving galaxies without emission lines, we obtain $M_{200a,\mathrm{dyn}} = 1.72^{+0.50}_{-0.47} \times 10^{15} h_{70}^{-1} M_\odot$. We note that the Evrard et al. (2008) scaling uses M_{200c} as the mass within a radius where the overdensity is 200 times the *critical* density of the universe, so the observed mass values reported in Sifón et al. (2012) have been scaled from critical to average density using $M_{200a} = 1.16^{+0.04}_{-0.03} \times M_{200c}$. This conversion factor was derived using a Navarro et al. (1997) mass profile (hereafter NFW) and the concentration–mass relation, $c(M,z)$, from simulations (Duffy et al. 2008) at $z = 0.87$ for the mass of the cluster. The reported uncertainties in the conversion factor reflect the $\sigma_{\log c} = 0.15$ scatter in the lognormal probability distribution of $c(M,z)$. The radius $r_{200} = 2111 \pm 189 h_{70}^{-1}$ kpc was also calculated using M_{200a} and assuming spherical symmetry, using the average density of the universe at redshift z, $\bar{\rho}(z) = \Omega_m(1+z)^3 3H_0^2/(8\pi G)$.

3.1.2. X-Ray Mass

We estimated the cluster mass from several X-ray mass proxies using the scaling relations in Vikhlinin et al. (2009) and Kravtsov et al. (2006). For the gas temperature and luminosity we essentially follow the prescriptions in Vikhlinin et al. (2009) to apply those scaling laws to the X-ray data. We obtain masses of $M_{500c} = 1.39^{+0.20}_{-0.19} \times 10^{15} h_{70}^{-1} M_\odot$ and $M_{500c} = 1.40^{+0.44}_{-0.36} \times 10^{15} h_{70}^{-1} M_\odot$ from the M_{500c}–T_{X} and M_{500c}–L_{X} relations, respectively. We refrain, however, from applying the 17% "merging cluster mass boost" as implemented by Vikhlinin et al. (2009), since, given the exceptional nature of ACT-CL J0102−4915, it is not obvious that such a correction

---

[19] See http://irsa.ipac.caltech.edu/data/SPITZER/docs/dataanalysistools/tools/contributed/irac/fixpulldown/

factor is appropriate. Owing to the complex substructure of the cluster, for the M_{gas}-based relations (Y_X and M_{gas}), we use the two-dimensional deprojection to generate an azimuthally average radial gas mass profile about the cluster center, which agrees well (within ~15%) with the azimuthally averaged core-excised surface brightness profile. For the Y_X mass proxy we obtain a mass of $M_{500c} = 1.55^{+0.15}_{-0.15} \times 10^{15} h_{70}^{-1} M_\odot$.

Since all of these mass proxies are potentially sensitive to merger boosts on T_X and L_X, we also explored using M_{gas}, which is intrinsically unaffected by merger boosts. However, the X-ray-derived measurement of M_{gas}, which comes from the reconstructed density by deprojecting the surface brightness, is sensitive to clumping. This can in principle result in a bias, depending on whether clusters are indeed more highly clumped during mergers. In the case of ACT-CL J0102−4915, the excellent agreement between our predicted SZ signal from the *Chandra* data and the actual millimeter-band ACT data suggests that gas clumping is not significant. We use the scaling law for M_{500c}−M_{gas} at redshift $z = 0.6$ from Kravtsov et al. (2006), which yields a value of $M_{500c} = 1.67^{+0.20}_{-0.20} \times 10^{15} h_{70}^{-1} M_\odot$ and implies a gas mass fraction $f_{gas} = 0.133$. The agreement among the four X-ray mass proxies is excellent: all are consistent within their 1σ ranges with a single mass value.

Our M_{200a} X-ray mass estimates are given in Table 2 using a conversion factor of $1.85^{+0.30}_{-0.20}$ from M_{500c} to M_{200a}. This factor is derived using the same procedure as in Section 3.1.1.

3.1.3. SZ Mass

We estimate the SZ-derived mass of this cluster using the peak Compton signal for the brightest $0\farcs5$ pixel (yT_{CMB}) of $490 \pm 60\,\mu K$ as published in Sehgal et al. (2011). We combined this measurement with a fiducial scaling relation between yT_{CMB} and M_{200a} derived from simulations and calibrated by X-ray observations with best-fit parameters given in that same work. Using this scaling relation, we find the mass of this cluster to be $M_{200,SZ} = 1.64^{+0.62}_{-0.42} \times 10^{15} h_{70}^{-1} M_\odot$. This mass is consistent with the independently derived mass reported by SPT (Williamson et al. 2011) of $M_{200,SZ} = (1.78 \pm 0.64) \times 10^{15} h_{70}^{-1} M_\odot$, which uses a similar scaling relation between the significance, ζ, and M_{200a}. This value also includes a 6% reduction to the published mass value to reflect the change in redshift from their photometric estimate ($z = 0.78$) to the true spectroscopic value ($z = 0.87$).

3.1.4. Stellar Mass from SED Fitting

In order to measure stellar population parameters and the stellar mass content of the cluster using galaxy members, we combine the optical photometry described in Section 2.2 with the IRAC photometry described in Section 2.5 by cross matching the catalogs using a $1\farcs2$ matching radius. We adopt the SExtractor MAG_AUTO measurements as estimates of total galaxy magnitudes in the optical bands and the $4''$ diameter aperture-corrected magnitudes as measurements of total flux in the IRAC bands.

We fit the broadband spectral energy distributions (SEDs) using a similar methodology to that described in Shapley et al. (2005; see also Hilton et al. 2010). We augmented the sample of 89 spectroscopic members to a total of 411 selected using photometric redshifts (Benítez 2000) re-calibrated with the 517 redshifts from seven clusters in the range $0.4 < z < 0.9$ from Sifón et al. (2012) and with the same *griz* photometry as ACT-CL J0102−4915. The improved photometric redshifts

had typical $\delta z = 0.04$ in the redshift range $0.8 < z < 0.9$. We select galaxies with photometric redshifts within $\Delta z \pm 0.06$ of the cluster mean redshift.

We construct a grid of Bruzual & Charlot (2003) solar metallicity models with exponentially declining star formation histories with 20 values of τ in the range 0.1–20 Gyr and 53 ages in the range 0.001–7.0 Gyr. We adopt a Chabrier (2003) initial mass function (IMF) and model the effect of dust extinction using the Calzetti et al. (2000) law, allowing $E(B - V)$ to vary in the range 0.0–0.5 in steps of 0.02. The SEDs are fitted by analytically calculating the normalization N for each model SED where $d\chi^2/dN = 0$, adopting the model with the lowest χ^2 value as the best fit. The stellar mass M_* is then estimated from the value of N. We therefore fit for a total of four parameters (age, τ, $E(B - V)$, M_*). Errors on the SED parameters were estimated using Monte Carlo simulations. Figure 7 shows some examples of fitted SEDs.

Given the small number of SED points compared with the number of free parameters, coupled with degeneracies between several parameters (age, τ, $E(B - V)$; see the discussion in Shapley et al. 2005), we do not expect the values of these parameters to be very robust. However, stellar mass is well constrained by the IRAC photometry, which probes the rest-frame near-IR at the cluster redshift, and stellar mass estimates have been shown to be fairly insensitive to variations in other model parameters, such as the assumed star formation history (e.g., Förster Schreiber et al. 2004; Shapley et al. 2005). We note that uncertainties in the IMF and the modeling of thermally pulsating asymptotic giant branch stars (e.g., Maraston 2005; Conroy et al. 2009) are likely to lead to the stellar mass estimates only being accurate to within a factor of two; these systematic uncertainties are not taken into account in quoted errors on M_*. The total stellar mass for all cluster members within $r_{200} = 2111\,h_{70}^{-1}$ kpc is $M_{200}^* = 1.31 \pm 0.26 \times 10^{13} M_\odot$. This suggests a ratio of stellar mass to total mass of <1% within r_{200} for ACT-CL J0102−4915.

3.2. Cluster Structure

In the ΛCDM paradigm, the dark matter distribution should be aligned with the distribution of galaxies if the dark matter particles are indeed collisionless. The cometary and bullet-like X-ray structure of ACT-CL J0102−4915 motivates our search for a spatial offset between the galaxies (that should primarily trace the dark matter distribution) and the X-ray gas in a cluster subcomponent as seen in, for example, 1E 0657−558 (Clowe et al. 2004), MS 1054−0321 (Jeltema et al. 2001), and MACS J0025.4−1222 (Bradač et al. 2008).

Our VLT campaign (Sifón et al. 2012) found no clear evidence for velocity substructure or a bimodal velocity distribution in ACT-CL J0102−4915. However, visual inspection of the optical images immediately suggested an elongated structure in the distribution of the red galaxies along the NW–SE axis, coincident with the direction of the structure seen in the X-ray emission (see Figure 1, left panels). We investigate the spatial cluster structure in more detail by constructing four maps: (1) the surface density of galaxies, (2) the i-band luminosity density, (3) the $3.6\,\mu m$/IRAC rest-frame luminosity density, and (4) the SED-fitted stellar mass density for spectroscopically and photometrically selected cluster members as described in Section 3.1.4. These four maps use a $6''$ pixel^{-1} grid smoothed with a Gaussian kernel of width $20''$. Figure 8 shows our deep optical multi-band imaging of ACT-CL J0102−4915 overplotted with yellow contours of the four density maps (one
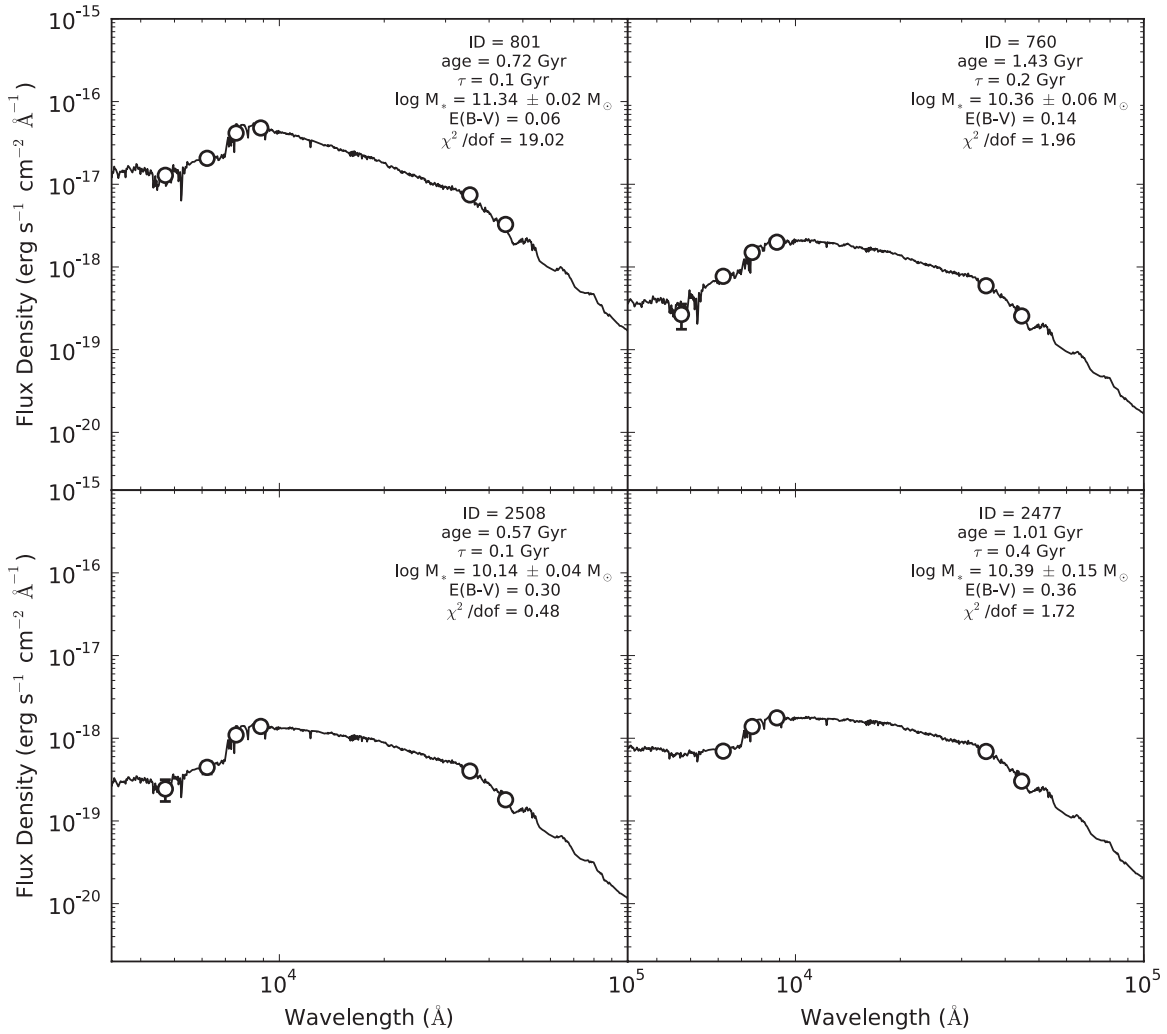
Figure 7. Examples of the SED fitting for four galaxy cluster members in ACT-CL J0102−4915. The solid line represents the best-fit SED for the broadband g, r, i, z, 3.6 μm and 4.5 μm photometry shown as open symbols.

per figure panel) along with the same X-ray surface brightness contours from Figure 1 displayed in white.

In all cases the galaxy distribution is obviously double peaked and a bright cD-type galaxy sits near each peak. For the galaxy density (Figure 8, upper left) and stellar mass density (lower right) maps, the peak of the X-ray emission lies between the peaks of the density. The luminosity densities for the i and 3.6 μm bands (Figure 8, upper right and lower left panels, respectively) are also double-peaked distributions. The i-band luminosity density, which probes the ultraviolet at $z = 0.87$, is somewhat unusual because it is dominated by the light contribution of the ultraluminous brightest cluster galaxy (BCG), discussed further below. As a result, the SE peak has the higher amplitude in the i band and coincides with the peak of the X-ray emission and with the location of the BCG. In the 3.6 μm band, which better traces the stellar mass, the NW peak is dominant, as with the galaxy number distribution. Note that the spatial distribution of the spectroscopically confirmed cluster members is also double peaked, similar to the contours in the top left panel of Figure 8.

Between and nearly equidistant from the two peaks in all four distributions lies a 20″ long straight blue arc, presumably the strongly lensed image of a high-redshift background galaxy (see

the black and white inset in Figure 1). This feature appears in the trough between the two peaks of all four distributions.

Regardless of whether we inspect the individual galaxies or their integrated light contribution, it is clear that there is a double-peak structure in their spatial distribution with nearly parallel contours that also align with the direction of the lensing arc. We use this feature to define two components in the cluster (which we refer to as the NW and SE components) and investigate their masses and differences in velocities of the components. Specifically, we divide cluster galaxies into two groups along the line defined by the pair of R.A. and decl. positions (01:03:22.0, −49:12:32.9) and (01:02:35.1, −49:18:09.8). The velocity dispersions of the NW and SE components are 1290 ± 134 and 1089 ± 200 km s^{-1}, respectively. We compute their masses using the same method described in Section 3.1.1 and obtain $1.76^{+0.62}_{-0.58} \times 10^{15}\, h_{70}^{-1}\, M_\odot$ and $1.06^{+0.64}_{-0.59} \times 10^{15}\, h_{70}^{-1}\, M_\odot$, respectively. Formally, this implies a range of possible mass ratios from approximately 5:1 to 1:1 between the cluster components; in subsequent analysis we will consider a 2:1 mass ratio. Table 1 gives computed values for the cluster components, as well as the cluster total. The sum of the masses of the two components determined separately, $(2.8 \pm 0.9) \times 10^{15}\, h_{70}^{-1}\, M_\odot$, is about 1$\sigma$ higher than the
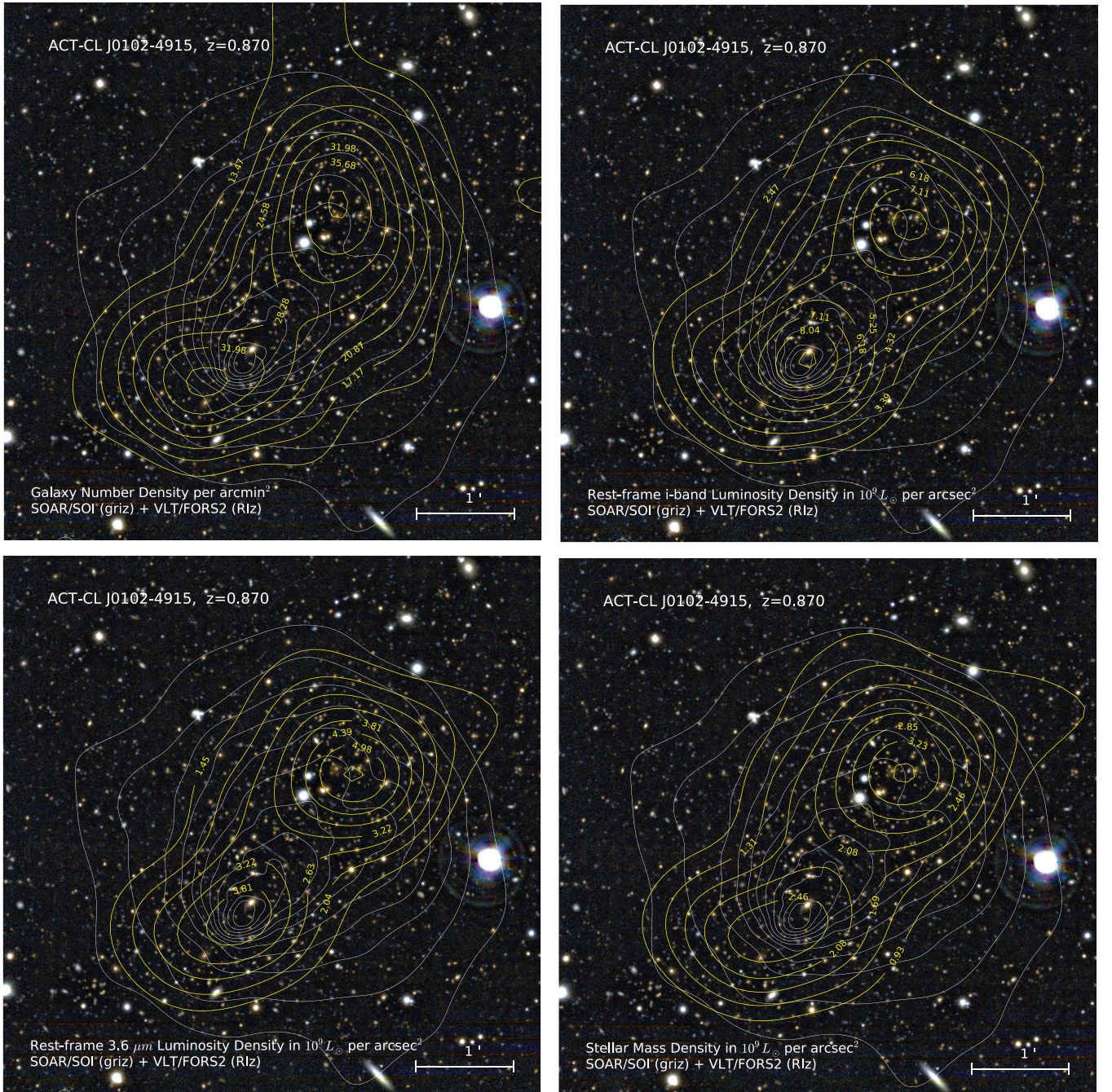
Figure 8. Isopleths from the joint spectroscopically and photometrically selected galaxies in ACT-CL J0102−4915 using four methods. The isopleth contours using (upper left) the number density of galaxies per square arcminute, (upper right) the rest-frame optical i-band luminosity, (lower left) the rest-frame 3.6 μm *Spitzer*/IRAC luminosity, and (lower right) the SED-fitted stellar mass. The luminosity contours are both in units of $10^9 L_\odot$ arcsec^{-2}, and the stellar mass map is in units of $10^9 M_\odot$ arcsec^{-2}. The X-ray emission is shown as white contours using the same levels from Figure 1. All panels agree on the bimodal structure of the galaxy distribution; moreover, both the galaxy number and stellar mass density maps have peaks with statistically significant offsets with respect to the X-ray emission peak.

(A color version of this figure is available in the online journal.)

Table 1
Dynamical Mass for ACT-CL J0102−4915 Components

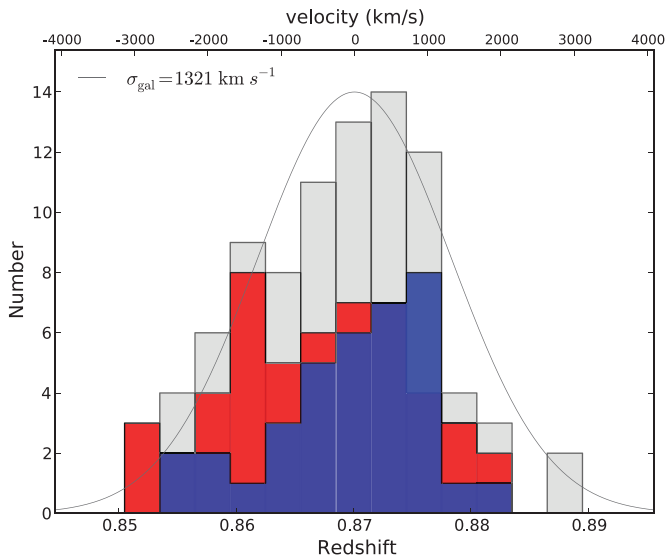| Group	$N_{\rm gal}$	Redshift	$\sigma_{\rm gal}$ (km s^{-1})	r_{200} (kpc h_{70}^{-1})	M_{200a} ($10^{15}\, h_{70}^{-1}\, M_\odot$)
ACT-CL J0102−4915 (NW)	51	0.86849 ± 0.00020	1290 ± 134	2062 ± 233	$1.76^{+0.62}_{-0.58}$
ACT-CL J0102−4915 (SE)	36	0.87175 ± 0.00024	1089 ± 200	1743 ± 336	$1.06^{+0.64}_{-0.59}$
ACT-CL J0102−4915 (total)	89	0.87008 ± 0.00010	1321 ± 106	2111 ± 189	$1.86^{+0.54}_{-0.49}$

Figure 9. Redshift distributions for spectroscopic member galaxies in the NW (red) and SE (blue) cluster subcomponent. The underlying distribution for all of the 89 cluster member galaxies for ACT-CL J0102−4915 is shown in gray.
(A color version of this figure is available in the online journal.)

Table 2
Mass Measurements for ACT-CL J0102−4915

Mass Proxy	Measurement	Scaling Law	M_{200a} $(10^{15} \, h_{70}^{-1} \, M_\odot)$
$\sigma_{\mathbf{gal}}$	1321 ± 106 km s^{-1}	M_{200}–σ	$1.86^{+0.54}_{-0.49}$
T_X	14.5 ± 1.0 keV	M_{500c}–T_X	$2.58^{+0.84}_{-0.59}$
L_X	2.19 ± 0.11	M_{500c}–L_X	$2.60^{+1.36}_{-0.87}$
Y_X	3.20 ± 0.24	M_{500c}–Y_X	$2.88^{+0.78}_{-0.55}$
M_{gas}	$2.2 \pm 0.1 \times 10^{14} \, M_\odot$	M_{500c}–M_{gas}	$3.10^{+0.92}_{-0.66}$
$yT_{\mathbf{CMB}}$	$490 \pm 60 \, \mu$K	M_{200}–y	$1.64^{+0.62}_{-0.42}$
Combined			$\mathbf{2.16 \pm 0.32}$

Notes. M_{500c} masses from L_X and T_X were scaled to M_{200a} masses assuming an NFW density profile and the mass–concentration relation of Duffy et al. (2008) as described in the text. L_X is in units of $10^{45} \, h_{70}^{-2}$ erg s^{-1} and is in the 0.5–2.0 keV band. Y_X is in units of $10^{15} \, M_\odot$ keV. The combined mass is the minimum χ^2 of the mass proxies in bold (σ_X, Y_X, and yT_{CMB}).

total cluster mass inferred from the velocity dispersion of all galaxies. We discuss this more in the next section.

The SE component has a line-of-sight peculiar velocity[20] of 586 ± 96 km s^{-1} with respect to the main (NW) component. We also note that the cluster BCG ($z = 0.87014 \pm 0.00030$), which is spatially located in the smaller SE mass component, has a peculiar velocity of 731 ± 66 km s^{-1} with respect to the main (NW) component. In Figure 9, we compare the distribution of the velocities for the NW and SE components shown in red and blue, respectively, against the distribution for the full sample.

We also use the cluster spatial information to obtain the stellar mass of the components with their respective r_{200} value using the SED fits from Section 3.1.4. Following the same component segregation as described above, we obtain stellar masses of $(7.5 \pm 1.4) \times 10^{12} \, M_\odot$ and $(5.6 \pm 1.3) \times 10^{12} \, M_\odot$ for the NW and SE components, respectively.

3.3. Combined Mass

Table 2 compiles our mass estimates for ACT-CL J0102−4915 from X-ray, SZ, and optical data sets. While central values range over nearly a factor of two, all estimates are statistically consistent. This can be seen by noting that the 2σ mass ranges for all six mass estimates overlap for the mass range 1.78×10^{15} to $2.88 \times 10^{15} \, h_{70}^{-1} \, M_\odot$; in other words, for any mass in this range, none of the six mass proxies are more than 2σ away. For a combined mass estimate on which to base further conclusions, we construct a χ^2 curve for a fit to a single combined mass value using the several mass estimates with their appropriate plus and minus error bars. For the three independent mass estimators from velocity dispersion, Y_X, and SZ decrement, we obtain a minimum χ^2 of 2.7 for 2 degrees of freedom (statistically acceptable) at a mass value of $M_{200a} = (2.16 \pm 0.32) \times 10^{15} \, h_{70}^{-1} \, M_\odot$. We do not combine all six mass proxies (which gives a somewhat higher mass value), since the four derived from the same X-ray data are all likely correlated to a degree that is difficult to evaluate.

The above error range includes uncertainties from measurement error, mass scaling relations, and extrapolation to a common M_{200a} mass scale. Estimates of galaxy cluster masses may also be impacted by a number of potential systematic errors. Since cosmological conclusions are strongly sensitive to the estimated cluster mass, it is important to have a realistic appraisal of these errors. Here we describe several relevant sources of systematic error or biases in both measured mass estimates and the theoretical comparison with cosmological models.

Dynamical mass estimates are based on the assumption that the system is dynamically relaxed, which is almost surely not the case in ACT-CL J0102−4915, based on the observed spatial galaxy distribution. If we are observing a merger with the component velocities primarily in the plane of the sky, then significant kinetic energy can be contained in motions transverse to the line of sight that are not observed in galaxy redshifts; the dynamically inferred mass would be lower than the actual system mass. This seems to be consistent with the measurements of the dynamical masses of the two subcomponents in ACT-CL J0102−4915 (explored in Section 3.2), which, when summed, $(2.8 \pm 0.9) \times 10^{15} \, h_{70}^{-1} \, M_\odot$, is in better agreement with the X-ray-derived masses than the full galaxy sample. Therefore, the dynamical mass of the full cluster quoted in Table 2 may be an underestimate.

A number of groups (e.g., Ricker & Sarazin 2001; Randall et al. 2002) have shown that cluster mergers can result in a transient boost in X-ray temperature and luminosity during a merger, compared to the X-ray emission of the merged cluster once it relaxes. The effect that such boosts have on the X-ray mass proxies has been more recently investigated by Kravtsov et al. (2006), Poole et al. (2007), and Yang et al. (2010), among others. Vikhlinin et al. (2009) argue that masses estimated from T_X should be *increased* by a factor of 1.17 (which we do not apply) for merger systems to account for the fraction of merger kinetic energy that remains unthermalized. Kravtsov et al. (2006) introduced the Y_X mass proxy, which has been shown to be fairly independent of merger dynamics (e.g., Kravtsov et al. 2006; Poole et al. 2007). ACT-CL J0102−4915 shows strong evidence for being in the merger process, particularly the compact region of X-ray enhancement and the double-peaked sky density distribution of galaxies. So in our combined mass estimate we strongly prefer to use Y_X, but we note that the masses for all the X-ray proxies are consistent with each other.

---

[20] This is estimated as $\Delta v = c(z_1 - z_2)/(1 + z_1)$, the peculiar velocity of the SE component in the reference frame of the NW component.

In particular, the agreement of our masses from the Y_X and M_{gas} proxies suggests that our X-ray masses are not significantly boosted by the merger.

The accuracy of the mass scaling law for the SZ proxy (here yT_{CMB}) is yet to be determined and in fact is one goal of the ACT follow-up program. Still it is interesting to note that the inferred SZ mass for ACT-CL J0102−4915 is only 60% of the Y_X-inferred mass, albeit consistent within the large errors. The excellent agreement we find between the predicted SZ signal from the *Chandra* and ACT data (as illustrated in Figure 6) suggests that we have a realistic gas model for the cluster and thus points to the mass scaling law, particularly at high redshift, as the main source of possible discrepancy. A similar difference between the SZ and X-ray derived masses is also seen for the massive cluster SPT-CL J2106−5844 at $z = 1.132$ (Foley et al. 2011), while Andersson et al. (2011) find that SZ-derived masses are some 22% less than their X-ray masses. Given six mass proxies for ACT-CL J0102−4915 that are all statistically consistent, it seems unlikely that our combined mass estimate is subject to significant systematic error.

For cosmological model comparisons, the theoretical mass function for clusters this massive is not precisely determined. In principle, direct numerical simulations of dark matter cosmology in large volumes and low-mass resolution can determine the high end of the mass function in a straightforward way. The largest simulations to date have comoving volumes of roughly 2000 Gpc^3, on the order of our Hubble volume, which nonetheless contain perhaps only a single cluster with mass $10^{15}\,M_\odot$ at $z = 1$. An analytical model of the high-mass mass function accurate at the 10% level has not yet been demonstrated, so the mass functions used for comparison involve extrapolation from lower mass halos where statistics from numerical simulations are better. Care also must be taken to ensure that initial conditions in simulations are sufficiently accurate; the commonly used Zeldovich Approximation for initial conditions may underestimate the number of high-mass halos by 10%–30% compared with more accurate second-order Lagrangian perturbation theory (Crocce et al. 2006; Berlind et al. 2010). Finally, large-volume simulations give dark matter halo masses, which then must be translated into total halo masses, with possible systematic departures from the commonly assumed universal baryon–to–dark matter ratio in large clusters.

3.4. Cluster Evolution

3.4.1. Color–Magnitude Relations

Considerable effort has been devoted to understanding the formation and evolution of ellipticals in clusters up to $z \simeq 1.4$ (e.g., Lidman et al. 2008; Hilton et al. 2009). A consistent picture has emerged in which these galaxies are a well-behaved class of objects with structural and chemical properties obeying simple power-law scaling relations. The high degree of homogeneity observed in these relations and in their stellar population suggests formation at high redshift followed by passive evolution of their galaxies (Bower et al. 1992; Barrientos et al. 1996; Ellis et al. 1997; Holden et al. 2005; Mei et al. 2009). In principle, when precise photometry is available, measurements of the intrinsic scatter about the color–magnitude relation (CMR) can be used to constrain the ages of the constituent stellar populations of cluster galaxies.

Here we study the optical and optical/IR CMRs for ACT-CL J0102−4915 to assess the evolutionary stage of the cluster. We construct the color–magnitude diagrams for spectro-
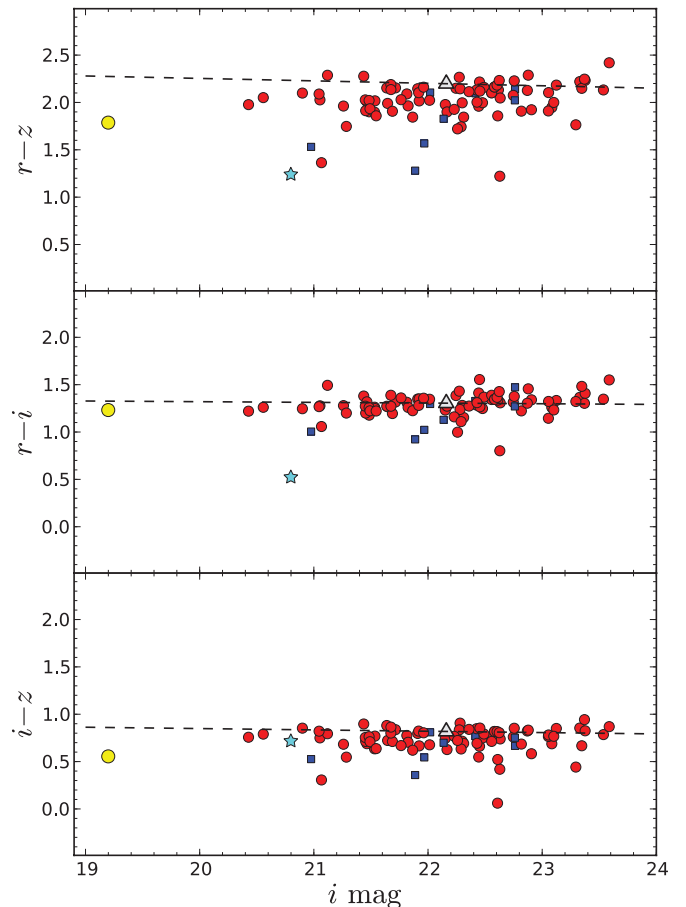

Figure 10. Optical CMRs for ACT-CL J0102−4915 for spectroscopically confirmed cluster members. Absorption- and emission-line galaxies are represented by red circles and blue squares, respectively, while the BCG is denoted by a yellow circle. The one spectroscopically confirmed AGN is represented by a cyan star. The dashed lines represent the fitted relations for the cluster RX J0152−1357 at $z = 0.83$ from Blakeslee et al. (2006) for the corresponding *HST*/ACS filters redshifted to $z = 0.87$. The gray triangle represents the observed magnitude of an M^* galaxy ($i = 22.16$) in the CMR.

(A color version of this figure is available in the online journal.)

scopically confirmed cluster members using the basic approach described in Blakeslee et al. (2006) and Menanteau et al. (2006). For total magnitudes, we use the SExtractor MAG_AUTO values (with a Kron factor of 2.5) and measure colors within the galaxy effective radii R_e that were computed using GALFIT (version 3.0; Peng et al. 2010) to fit each galaxy to a Sersic (1968) model from the point-spread function convolved i-band images. Bright nearby objects are fit simultaneously while faint ones are masked. Magnitudes in each passband are then measured within a circular aperture of radius R_e while enforcing a minimum radius of 1.5 pixels.

In Figures 10 and 11, we show the optical and optical-to-infrared color–magnitude diagrams for spectroscopically confirmed cluster members. Absorption- and emission-line galaxies are represented by red circles and blue squares, respectively, while the BCG is denoted by a larger yellow circle. In order to ease the comparison between panels, all colors are shown with respect to the total i-band magnitude. In order to compare with the expected colors of the passively evolving system in Figure 10, we show for comparison the fitted optical CMRs for the cluster RX J0152−1357 at $z = 0.83$ from Blakeslee et al. (2006), which was observed with the corresponding *Hubble Space Telescope*
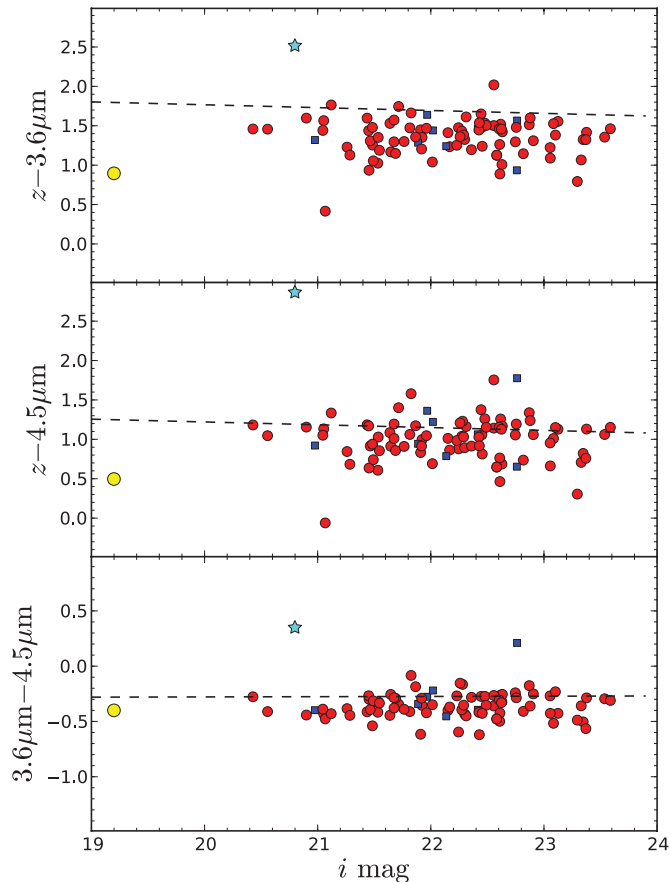
Figure 11. Optical-to-infrared color–magnitude diagram for cluster member galaxies. Symbols are as in Figure 10. The dashed lines again represent the fitted relations for the cluster RX J0152−1357 at $z = 0.83$ from Blakeslee et al. (2006), now transformed to the *Spitzer*/IRAC bands as described in the text.

(A color version of this figure is available in the online journal.)

Figure 12. Observed *i*-band magnitudes for the BCGs in the SZ cluster sample reported in Menanteau et al. (2010a) compared with the BCGs of several high-redshift clusters. We highlight the BCG of ACT-CL J0102−4915 as a yellow star. For comparison we show the curves for the expected *i*-band magnitude as a function of redshift for elliptical galaxies over a wide range of intrinsic luminosities (i.e., the curves represent the observed magnitude for galaxies of the same luminosity).

(A color version of this figure is available in the online journal.)

(*HST*)/Advanced Camera for Surveys (ACS) filter set and redshifted to $z = 0.87$ using a solar metallicity Bruzual & Charlot (2003) burst model with $\tau = 1.0$ Gyr formed at $z_f = 5$. We also display for reference the typical magnitude for an M^* ($i = 22.16$) galaxy at the cluster redshift in the CMR as a gray triangle. In Figure 11, we show the fitted $i - z$ versus i relation from Figure 10 transformed to the *Spitzer*/IRAC band using the same stellar population model.

Despite some scatter, a "red sequence" of passively evolved galaxies is quite distinguishable and is in good agreement with the observed relations for RX J0152−1357. However, unlike Blakeslee et al. (2006), we see bluer early-type galaxies brighter than M^* possibly owing to recent star formation triggered by the merger of the cluster. We note, however, that our classification of galaxies is only based on the color and visual information in our seeing-limited ground-based imaging.

From the figures it is also clear that the BCG is extremely luminous (∼1.5 mag brighter than any other galaxy) and significantly bluer in its optical colors than expected from a passively evolving elliptical galaxy. In the following section, we describe the BCG properties in more detail.

3.4.2. Luminosity of Brightest Central Galaxy

In Figure 12, we plot the observed *i*-band magnitude of the BCGs of ACT clusters in the southern sample, plus the BCGs for three X-ray-selected, massive, high-redshift clusters: RDCS 1252.9−2927 (Blakeslee et al. 2003; Rosati et al. 2004;
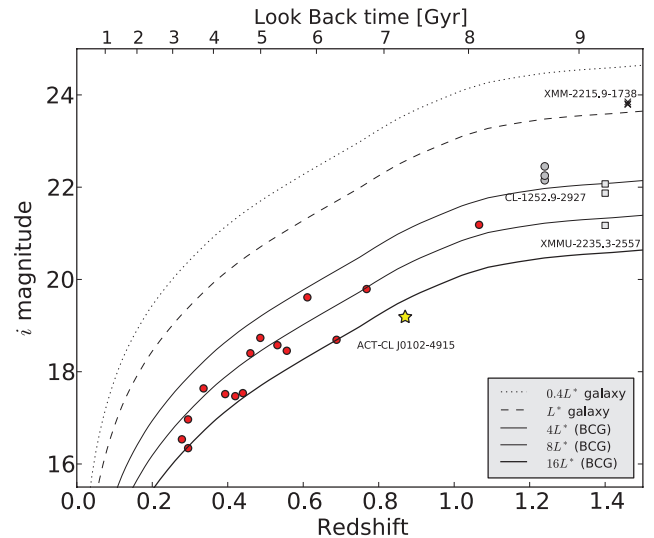
Demarco et al. 2007) at $z = 1.237$, XMMU J2235.3−2557 (Mullis et al. 2005; Rosati et al. 2009) at $z = 1.393$, and XM-MXCS J2215.9−1738 (Stanford et al. 2006; Hilton et al. 2009) at $z = 1.457$. For clarity the BCG for ACT-CL J0102−4915 is shown as the yellow star, with a luminosity of $\simeq 22L^*$ in the *i* band. This is clearly an extremely luminous object and is the brightest BCG in the ACT southern sample. We also plot the expected apparent *i*-band magnitudes of elliptical galaxies of different luminosities as a function of redshift. We use L^* in the *i* band as defined by Blanton et al. (2003) at $z = 0.1$ ($M_i^* = -20.82 + 5 \log(0.7)$) and allow passive evolution according to a solar metallicity, Bruzual & Charlot (2003) $\tau = 1.0$ Gyr burst model formed at $z_f = 5$. The resulting magnitude–redshift relation is plotted for a range of luminosities ($0.4L^*$, L^*, $4L^*$, $8L^*$, and $16L^*$) aimed at representing the brightest observed BCGs.

The VLT/FORS2 spectrum of the BCG in ACT-CL J0102−4915 has the signature of an E+A+[O II] galaxy. This galaxy is a possible high-redshift analog of NGC 1275, the blue and radio-loud cD galaxy in the Perseus Cluster at $z = 0.018$ (McNamara et al. 1996). Blue BCGs like this one usually live in the centers of cool-core clusters (e.g., Santos et al. 2011), and in this case the BCG is located within the cool, low-entropy, merging core in ACT-CL J0102−4915 revealed by the *Chandra* data. We also obtain the physical size of the BCG from the structural parameters estimated using GALFIT in Section 3.4.1. The galaxy has an effective radius $R_e = 10.4\,h_{70}^{-1}$ kpc for a Sérsic index $n = 1.3$. It is likely that this BCG is the result of a recent galaxy merger; we speculate that this extreme galaxy resulted from a merger of two BCGs during the cluster collision.

4. DISCUSSION

4.1. A New Bullet Cluster?

Given the absence of a weak-lensing mass reconstruction, we use the galaxy distribution as a proxy for the total mass
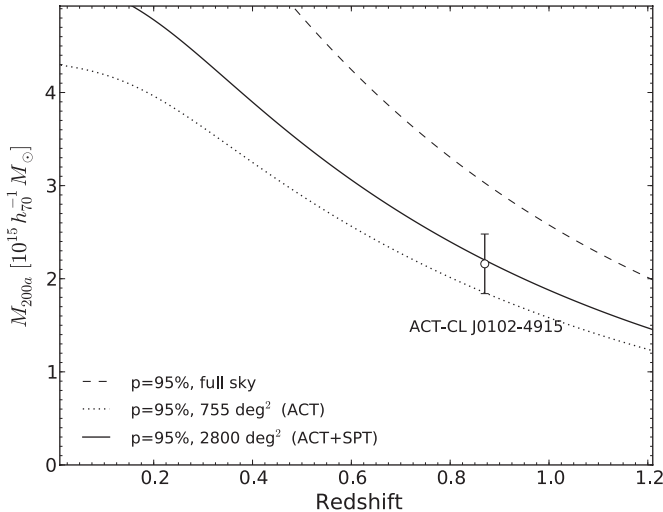
13

Figure 13. Exclusion curves, $M_{200a}(z)$, from the Mortonson et al. (2011) fitting formulas where a single cluster above the corresponding curve would conflict with flat ΛCDM and quintessence at 95% CL for both sample and parameter variance. The black dashed and dotted lines represent the exclusion curves for the full sky and the ACT survey analyzed region of 755 deg² (i.e., the mass limit for a cluster at a given redshift that it is less than 5% likely to be found in 95% of the ΛCDM parameter probability distribution). We also show the same exclusion limit for 2800 deg² (ACT+SPT area) as the black solid curve. The open circle shows our combined mass estimate for ACT-CL J0102−4915, with 1σ error bars.

distribution. This should be a robust approximation since for both 1E 0657−56 (Randall et al. 2008) and MACS J005.4−1222 (Bradač et al. 2008) the galaxy and total matter distribution closely track each other. Figure 8 (upper left panel) shows that the SE galaxy distribution precedes the peak gas location by $\simeq 22''$ (173 h_{70}^{-1} kpc) in the approximate direction of motion of the merger. This suggests ACT-CL J0102−4915 as another "bullet" cluster undergoing a high-velocity merger event resulting in a significant spatial separation in the main baryonic (gas) and total mass components. Moreover, ACT-CL J0102−4915 is at a significantly earlier cosmic epoch, a look-back time around 4 Gyr longer than 1E 0657−56. However, this picture requires confirmation through weak-lensing mass mapping to determine the spatial distribution of the dark matter.

4.2. Rarity of ACT-CL J0102−4915

ACT-CL J0102−4915 is a rare, massive high-redshift cluster. We use the convenient fitting formulas provided in Appendix A of Mortonson et al. (2011) to compute the confidence level (CL) at which the existence of a cluster like ACT-CL J0102−4915 would be expected in standard ΛCDM cosmological models, where bound objects grow via gravitational instability from Gaussian initial density fluctuations. In Figure 13, we show $M_{200a}(z)$ exclusion curves for which a single cluster with mass M_{200a} above the corresponding curve would conflict with ΛCDM and quintessence at 95% CL, including both sample and cosmological parameter variance. In other words, the exclusion curves represent the mass threshold as a function of redshift for which a cluster is less than 5% likely to be found in a survey region for 95% of the ΛCDM parameter variance.

For purposes of addressing how rare ACT-CL J0102−4915 is, in Figure 13 we plot the exclusion curves for the full sky, the region analyzed for the ACT survey (755 deg²) where ACT-CL J0102−4915 was discovered, and the combined ACT+SPT survey region (2800 deg², of which 455 deg² were

observed by both ACT and SPT), as this is the most massive cluster at $z > 0.5$ in the combined area and detected by both experiments. Our combined estimated 1σ mass range for the cluster (in Table 2) ranges from 1.84×10^{15} to $2.48 \times 10^{15} \, h_{70}^{-1} \, M_{\odot}$. At the cluster redshift of 0.87, the lower end of this mass range falls below the ACT+SPT region exclusion curve, while the upper end of this range falls well below the full-sky exclusion curve. In other words, the cluster is not an unlikely occurrence in the ACT+SPT sky region, provided that its actual mass is 1σ or more below our nominal mass of $2.16 \times 10^{15} \, h_{70}^{-1} \, M_{\odot}$. If the cluster mass is 1σ–2σ above this nominal mass, then it is a rare occurrence in the ACT+SPT sky region but not unexpected in the entire sky. The cluster mass would have to be about 3σ above the nominal mass for it to lie above the 95% exclusion curve for the entire sky. We conclude that, while this cluster is clearly rare, it is not massive or early enough to put significant pressure *by itself* on the standard cosmological model.

Because the high-mass cluster mass function is steeply falling with mass, the signals we observe are more likely to be from a cluster with mass below our nominal mass of $2.16 \times 10^{15} \, h_{70}^{-1} \, M_{\odot}$ and a positive measurement error than from a cluster with mass above this level and a negative measurement error. In other words, the cluster mass is more likely to be near the lower end of our nominal mass range than the upper end. Lima & Hu (2005) give a discussion of this Eddington bias and compute a correction for this effect, which in our case is of order 5%. This correction does not qualitatively change any conclusions presented here.

Lee & Komatsu (2010) investigated the rarity of 1E 0657−558 in cosmological simulations down to $z < 0.5$ based on its large merger velocity and found the existence of such a merging cluster to be in tension with the expectations of ΛCDM. They suggested that such high merger speeds could potentially be more common at high redshift, while, on the other hand, massive, $\sim 10^{15} \, M_{\odot}$, clusters are rare at earlier times. Using simulations, Forero-Romero et al. (2010) studied the expected probability distribution of the displacements between the dark matter and gas cores, as observed in 1E 0657−558, and found it to be expected in 1%–2% of the clusters with masses larger than $10^{14} \, M_{\odot}$.

Here we briefly consider the rarity of ACT-CL J0102−4915 as a massive cluster undergoing a major merger with a mass ratio of ~ 2 to 1 at $z = 0.87$, ignoring its merger velocity and spatial separation between gas and dark matter. We examined the output of a large-volume $(3.072 \, h^{-1} \, \text{Gpc})^3$ ΛCDM cosmological N-body simulation with 29 billion particles performed by I. Iliev with the Cubep3m code at NIC Juelich (G. Yepes 2011, private communication). Within this large volume there is only one cluster of mass $1.9 \times 10^{15} \, h_{70}^{-1} \, M_{\odot}$ at $z \simeq 1$, which implies a very low number density of around 10^{-11} Mpc^{-3} for such clusters. This system has only one small potential substructural feature with a mass of around $10^{13} \, M_{\odot}$, suggesting a recent minor merger with mass ratio of 100 to 1. The comoving volume of the entire sky between $z = 0$ and $z = 1$ is 54.7 h^{-3} Gpc^3, and hence the examined simulation samples roughly half of the total cosmic volume accessible by SZ cluster observations. We conclude that a merger event of the mass and mass ratio similar to the one we are witnessing in ACT-CL J0102−4915 is a rare event in the current set of large-volume simulations. Significantly larger simulations, or improved analytic approximations to halo growth and evolution, will be required to assess directly the likelihood of massive high-redshift merger events such as ACT-CL J0102−4915.
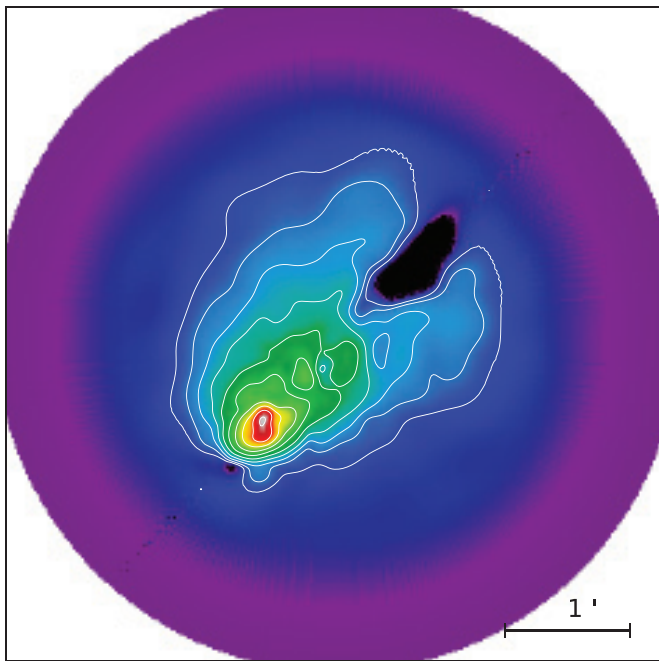
Figure 14. Map of the electron density in the mid-plane of ACT-CL J0102−4915 from a deprojection of the *Chandra* image. The contours are at density values of 0.002, 0.003, 0.004, 0.006, 0.008, 0.011, 0.016, 0.023, 0.032, and 0.045 cm^{-3}.
(A color version of this figure is available in the online journal.)

4.3. Merger Speed

We have argued above that the depression in the X-ray surface brightness northwest of the merging bullet is a "wake" caused by the passage of one cluster through the other. In order to study this feature in more detail, we examine the map of the deprojected electron density in the cluster mid-plane (i.e., the plane of the sky) of ACT-CL J0102−4915 (see Figure 14). The merging bullet is indeed dense with a peak density of $n_e = 0.047$ cm^{-3}, while the outskirts fall to a value $n_e \simeq 2 \times 10^{-4}$ cm^{-3}. Formally, our simple deprojection procedure fails in the region of depressed surface brightness (presumably because the cluster is not axially symmetric as assumed), and the density values here were pegged to zero; this area appears black in Figure 14.

Nonetheless, clearly the NW region of depressed X-ray surface brightness requires a region of extremely low density in the cluster interior. The region of depressed density is about $0\rlap{.}'8$–$1'$ ($370\, h_{70}^{-1}$–$460\, h_{70}^{-1}$ kpc) wide. It begins approximately $2\rlap{.}'6$ ($1200\, h_{70}^{-1}$ kpc) behind the leading edge of the bullet toward the northwest and can be traced into the core of the cluster to within about $1'$ ($460\, h_{70}^{-1}$ kpc) from the bullet. At locations even closer to the bullet, the deprojected density map shows a complex, disorganized set of peaks and valleys, suggesting the presence of merger-driven turbulence behind the cold merging core.

The merger speed can be estimated from the peculiar velocity difference between the SE and NW galaxy concentrations as $v_{\rm merg} = v_{\rm pec}/\sin(\theta) = 586/\sin(\theta)$ km s^{-1}. The collision is likely taking place close to the plane of the sky; otherwise, the clear morphological features of that merger, i.e., sharp leading edge, post-bullet turbulence, and the wake (Figure 14), would not be so prominent. Working from this scenario, we assume low inclination angles of $\theta = 15°$ and $30°$ that provide merger speeds of 2300 km s^{-1} and 1200 km s^{-1}. An accurate estimate of the merger speed will require detailed N-body/hydro simulations.

4.4. Extended Radio Emission around ACT-CL J0102−4915?

There is increasing observational evidence (see Ferrari et al. 2008 for a review) that the large amount of energy released ($\sim 10^{64}$ erg) in massive cluster mergers can accelerate particles to relativistic speeds that in the presence of an intracluster magnetic field can produce synchrotron radiation. These diffuse, non-thermal emission features, called radio relics or halos, have no obvious connection with individual cluster galaxies and have typical sizes of about 1 Mpc. We searched for such radio features around ACT-CL J0102−4915 using Sydney University Molonglo Sky Survey (SUMSS) archival data at 843 MHz. The radio mosaic at the cluster location has an angular resolution of $45'' \times 60''$ (major axis aligned N–S) and a positional uncertainty for bright sources (>20 mJy beam^{-1}) of $1''$–$2''$ (Mauch et al. 2003). In Figure 15 (right panel), we show the SUMSS archival map with the location of three radio sources, labeled A, B, and C, indicated with blue crosses (see Table 3). Only source A was cataloged in Mauch et al. (2003); the latter two sources (B and C) were analyzed by us using IMFIT within the Astronomical Image Processing System (AIPS). Under the assumption that the typical position error for faint sources scales as the beam size times the signal-to-noise ratio, we estimate positional errors for sources B and C of $\sim 7''$, which we use in the search for possible counterparts (galaxies; active galactic nuclei, AGNs) in our optical and X-ray data. There is an excellent compact optical, IR, and X-ray counterpart for source B ($<1''$ away), making an AGN identification for this source likely. The nearest X-ray source to position C is $8''$ away, which is at the limit of the radio source positional uncertainty, so a clear identification is not possible. Furthermore, this radio source is located right at the apex of the merging bullet, at the plausible location of a bow shock. There is no plausible X-ray counterpart for source A, which is also extended approximately in the direction perpendicular to the merger axis and centered near where the countershock should appear. Moreover, Figure 15 (left panel), an unsharp-masked image of the *Chandra* data (the difference of two images convolved with two-dimensional Gaussian smoothing widths of $\sigma = 7\rlap{.}''5$ and $30''$), reveals high-frequency structure, i.e., a sharp edge to the X-ray surface brightness, at the locations of both radio sources A and C, lending credence to the idea that we are seeing radio relics similar to those seen in several nearby clusters, such as A3667 (Rottgering et al. 1997), A3376 (Bagchi et al. 2006), and A1240 (Kempner & Sarazin 2001), that are believed to be powered by merger shocks (see, e.g., van Weeren et al. 2011). Kempner et al. (2004) suggest the term *radio gischt* for these features to distinguish them from other types of radio sources in clusters, such as AGN relics and radio phoenix sources.

The monochromatic radio power of source A, assuming it is located at the redshift of the cluster, is $P_{1.4} = 7 \times 10^{25}$ W Hz^{-1}. Likewise, the radio power of source C is $P_{1.4} = 3 \times 10^{25}$ W Hz^{-1}. The rest-frame frequency of the 843 MHz observations at the redshift of ACT-CL J0102−4915 is 1.576 GHz, which we multiply by a factor of 1.126 to convert to the monochromatic power at rest-frame frequency 1.4 GHz, which assumes a spectral index of −1. The radio power of source A is one of the most intense known among radio gischt sources. Feretti (2002) shows that the radio power of gischt relics correlates with the cluster bolometric X-ray luminosity (albeit with large scatter). The high radio power and bolometric X-ray luminosity of ACT-CL J0102−4915 put it at the extreme upper end of this correlation. For ACT-CL J0102−4915, an important caveat
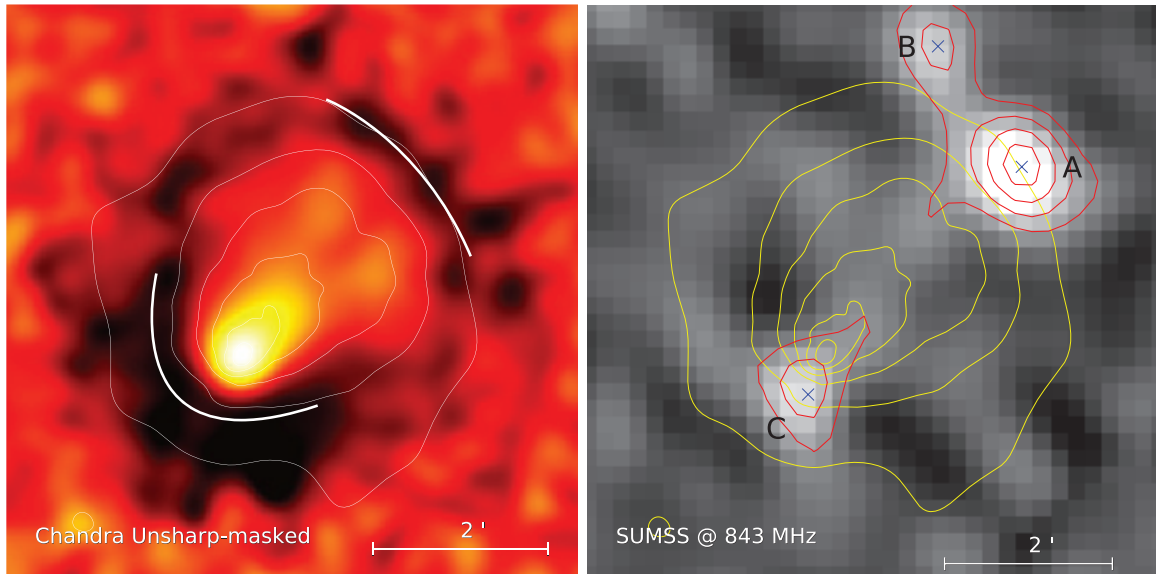
Figure 15. Unsharp-masked *Chandra* 0.5–2.0 keV image for ACT-CL J0102−4915 created from the subtraction of two images convolved with Gaussians of $\sigma = 7''.5$ and $30''$ with the high-frequency features highlighted as thick white curves (left). The SUMSS 843 MHz image of the same region showing the position of the radio sources A, B, and C on the map and their respective contours level are shown in red (right). In both images and for reference we overlay the same X-ray contours used in Figure 5.

(A color version of this figure is available in the online journal.)

Table 3
Summary of SUMSS Radio Source Positions and Fluxes near ACT-CL J0102−4915

Source	Name	R.A.	Decl.	F_ν(mJy)	Size	P.A.	In SUMSS
A	SUMSS J010246-491435	01:02:46.8	−49:14:35.7	18.2 ± 1.5	$70'' \times 59''$	$64°$	Yes
B	SUMSS J010252-491316	01:02:52.4	−49:13:16.7	7.2 ± 1.2	Unresolved	$\cdots$	No
C	SUMSS J010301-491705	01:03:01.1	−49:17:05.0	7.8 ± 1.2	Unresolved	$\cdots$	No

Notes. Only the first object (A) was cataloged; the latter two sources were analyzed by us using IMFIT (AIPS) on the mosaic image. Sources are ordered in increasing right ascension.

of our interpretation of the SUMSS measurements is that the angular resolution of the radio images is insufficient to identify and remove radio source contamination, so the values of radio power quoted above for sources A and C should be considered upper limits to the diffuse radio emission. Approved observations at the Australia Telescope Compact Array (ATCA) will provide higher resolution imaging that will help to remove much of this uncertainty due to unresolved radio source emission at the site of the relics. If confirmed, this will be the most distant radio relic observed.

5. SUMMARY AND CONCLUSIONS

We present a multi-wavelength analysis of ACT-CL J0102−4915 "El Gordo," a new SZ cluster that appears to be the first reported high-redshift Bullet-like cluster undergoing a major merger. We have used a combination of optical (VLT), X-ray (*Chandra*), and infrared (*Spitzer*) data to investigate the cluster's physical properties and find that it is an exceptionally massive, X-ray luminous, and hot system, resulting in the highest SZ signal in the ACT survey. From the optical spectra of 89 galaxies confirmed as cluster members, we obtain a spectroscopic redshift ($z = 0.87008$) and velocity dispersion ($\sigma_{\rm gal} = 1321 \pm 106$ km s^{-1}) for this cluster. Our 60 ks *Chandra* observation on ACIS-I provides a spectroscopic temperature of $T_{\rm X} = 14.5 \pm 1.0$ keV and bolometric luminosity of $L_{\rm bol} = 13.6 \times 10^{45} h_{70}^{-2}$ erg s^{-1}. From mass scaling relations for the

velocity dispersion, X-ray $Y_{\rm X}$, and SZ distortion, we determine the total mass of the cluster to be $M_{200a} = (2.16 \pm 0.32) \times 10^{15} h_{70}^{-1} M_\odot$, establishing it as the most massive cluster known at $z > 0.6$.

From our warm-phase *Spitzer* IRAC and deep optical imaging, we measure the total stellar mass and constrain the stellar content of the cluster to be <1% of the total mass, in broad agreement with other massive clusters. The optical (riz bands) and IR (3.6 μm, 4.5 μm) color–magnitude diagrams for spectroscopically confirmed members show a clearly defined red sequence consistent with passively evolving galaxies, including a small fraction of actively star-forming galaxies. However, the BCG is extremely luminous, significantly bluer than the red sequence, and appears as an E+A+[O II] galaxy from the VLT spectra. Such blue BCGs are normally seen in the centers of cool-core clusters, and indeed this BCG sits right within the cool, low-entropy, enhanced-metal-abundance merging core in ACT-CL J0102−4915 revealed by the *Chandra* data.

While clusters as massive as ACT-CL J0102−4915 are quite rare at its redshift, the cluster does not pose any significant difficulty for the standard ΛCDM cosmology provided that its mass is in the lower portion of its statistically allowed mass range. Our *Chandra* and VLT observations additionally show that ACT-CL J0102−4915 is undergoing a major merger with a mass ratio of approximately 2 to 1 between its subcomponents. We find no analogous high-mass merging systems, with

properties broadly similar to ACT-CL J0102−4915, within any current large-volume cosmological *N*-body simulations (e.g., MICE, Cubep3m). Thus, the high mass and merger ratio at this redshift argues for an exceptional rarity of ACT-CL J0102−4915 within our universe. We expect that more detailed analysis of large cosmological simulations and better understanding of the propagation of the initial Gaussian fluctuations, particularly at high redshift, will be required to compare with the predictions of a ΛCDM model using massive systems like ACT-CL J0102−4915.

The X-ray surface brightness of our *Chandra* observation reveals a "wake" in the hot gas distribution that we attribute to the recent passage of one cluster through the other. The deprojected gas density distribution shows that the wake requires a low-density cavity in the interior of the cluster. Understanding the evolution of these features, determining the merger speed, and quantifying the rarity of a merging cluster system with the relative masses and velocities of the subcomponents of ACT-CL J0102−4915 will require further simulations and analysis.

Inspection of archival SUMSS radio observations at 843 MHz reveals the presence of radio sources located at the southeast and northwest edges of the cluster, which we tentatively identify as radio gischt relics hosted by ACT-CL J0102−4915. They lack obvious X-ray counterparts, and their positions relative to the cluster are consistent with the expected locations of merger-induced shocks. The northwestern radio source is intense ($P_{1.4} = 7 \times 10^{25}$ W Hz^{-1}) and is extended perpendicular to the merger direction. If upcoming ATCA observations confirm the diffuse nature of the radio emission, then ACT-CL J0102−4915 will be the highest redshift cluster with a radio gischt relic.

The next most critical observational step is to obtain strong- and weak-lensing mass estimates and maps from the ground and with the *HST*, which we are pursuing. This will allow us to confirm the presence of an offset between the baryonic and dark matter distributions, as well as provide a robust mass estimate unbiased by merger state or cluster astrophysics. A deeper approved *Chandra* observation will allow better mapping of the spatial temperature distribution in the cluster, which may allow identification of shocks in the gas. It is now possible to use ALMA to search for these same features directly in the SZ effect using the low-frequency channel (Band 3 covering 84–116 GHz). Confirmation of the radio relic is clearly a high priority since these are typically found in merging clusters; moreover, ACT-CL J0102−4915's high redshift will allow investigation of their cosmic evolution. As we have outlined above, several theoretical steps also need to be pursued in order to fully understand the many distinctive features of ACT-CL J0102−4915 that we have presented here. We hope that this new exceptional cluster will fuel more in-depth simulations of cluster mergers and motivate continued searches for similar high-redshift systems.

REFERENCES

Abazajian, K. N., Adelman-McCarthy, J. K., Agüeros, M. A., et al. 2009, ApJS, 182, 543

AMI Consortium: Rodríguez-Gonzálvez, C., Olamaie, M., Davies, M. L., et al. 2011, MNRAS, 414, 3751

Andersson, K., Benson, B. A., Ade, P. A. R., et al. 2011, ApJ, 738, 48

Bagchi, J., Durret, F., Neto, G. B. L., & Paul, S. 2006, Science, 314, 791

Barmby, P., Huang, J.-S., Ashby, M. L. N., et al. 2008, ApJS, 177, 431

Barrientos, L. F., Schade, D., & Lopez-Cruz, O. 1996, ApJ, 460, L89

Beers, T. C., Flynn, K., & Gebhardt, K. 1990, AJ, 100, 32

Benítez, N. 2000, ApJ, 536, 571

Berlind, A. A., Farrar, G. R., & Zaw, I. 2010, ApJ, 716, 914

Bertin, E. 2006, SWarp Resample and Coadd Software, http://terapix.iap.fr/cplt/oldSite/soft/swarp/index.html

Bertin, E., & Arnouts, S. 1996, A&AS, 117, 393

Blakeslee, J. P., Franx, M., Postman, M., et al. 2003, ApJ, 596, L143

Blakeslee, J. P., Holden, B. P., Franx, M., et al. 2006, ApJ, 644, 30

Blanton, M. R., Hogg, D. W., Bahcall, N. A., et al. 2003, ApJ, 592, 819

Bower, R. G., Lucey, J. R., & Ellis, R. S. 1992, MNRAS, 254, 601

Bradač, M., Allen, S. W., Treu, T., et al. 2008, ApJ, 687, 959

Bruzual, G., & Charlot, S. 2003, MNRAS, 344, 1000

Calzetti, D., Armus, L., Bohlin, R. C., et al. 2000, ApJ, 533, 682

Carlstrom, J. E., Ade, P. A. R., Aird, K. A., et al. 2009, PASP, 123, 568

Chabrier, G. 2003, PASP, 115, 763

Clowe, D., Bradač, M., Gonzalez, A. H., et al. 2006, ApJ, 648, L109

Clowe, D., Gonzalez, A., & Markevitch, M. 2004, ApJ, 604, 596

Conroy, C., Gunn, J. E., & White, M. 2009, ApJ, 699, 486

Crocce, M., Pueblas, S., & Scoccimarro, R. 2006, MNRAS, 373, 369

Demarco, R., Rosati, P., Lidman, C., et al. 2007, ApJ, 663, 164

Dressler, A., & Shectman, S. A. 1988, AJ, 95, 985

Duffy, A. R., Schaye, J., Kay, S. T., & Dalla Vecchia, C. 2008, MNRAS, 390, L64

Ellis, R. S., Smail, I., Dressler, A., et al. 1997, ApJ, 483, 582

Evrard, A. E., Bialek, J., Busha, M., et al. 2008, ApJ, 672, 122

Feretti, L. 2002, in IAU Symp. 199, The Universe at Low Radio Frequencies, ed. A. Pramesh Rao, G. Swarup, & Gopal-Krishna (Cambridge: Cambridge Univ. Press), 133

Ferrari, C., Govoni, F., Schindler, S., Bykov, A. M., & Rephaeli, Y. 2008, Space Sci. Rev., 134, 93

Foley, R. J., Andersson, K., Bazin, G., et al. 2011, ApJ, 731, 86

Forero-Romero, J. E., Gottlöber, S., & Yepes, G. 2010, ApJ, 725, 598

Förster Schreiber, N. M., van Dokkum, P. G., Franx, M., et al. 2004, ApJ, 616, 40

Fowler, J. W., Acquaviva, V., Ade, P. A. R., et al. 2010, ApJ, 722, 1148

Fowler, J. W., Niemack, M. D., Dicker, S. R., et al. 2007, Appl. Opt., 46, 3444

Girardi, M., Demarco, R., Rosati, P., & Borgani, S. 2005, A&A, 442, 29

Haehnelt, M. G., & Tegmark, M. 1996, MNRAS, 279, 545

Hilton, M., Lloyd-Davies, E., Stanford, S. A., et al. 2010, ApJ, 718, 133

Hilton, M., Stanford, S. A., Stott, J. P., et al. 2009, ApJ, 697, 436

Hincks, A. D., Acquaviva, V., Ade, P. A. R., et al. 2010, ApJS, 191, 423

Holden, B. P., Blakeslee, J. P., Postman, M., et al. 2005, ApJ, 626, 809

Jee, M. J., & Tyson, J. A. 2009, ApJ, 691, 1337

Jeltema, T. E., Canizares, C. R., Bautz, M. W., et al. 2001, ApJ, 562, 124

Katgert, P., Mazure, A., Perea, J., et al. 1996, A&A, 310, 8

Kempner, J. C., Blanton, E. L., Clarke, T. E., et al. 2004, in The Riddle of Cooling Flows in Galaxies and Clusters of Galaxies, ed. T. Reiprich, J. Kempner, & N. Soker (Charlottesville, VA: Univ. Virginia), 335

Kempner, J. C., & Sarazin, C. L. 2001, ApJ, 548, 639

Kravtsov, A. V., Vikhlinin, A., & Nagai, D. 2006, ApJ, 650, 128

Kurtz, M. J., & Mink, D. J. 1998, PASP, 110, 934

Lee, J., & Komatsu, E. 2010, ApJ, 718, 60

Lidman, C., Rosati, P., Tanaka, M., et al. 2008, A&A, 489, 981

Lima, M., & Hu, W. 2005, Phys. Rev. D, 72, 043006

Makovoz, D., & Khan, I. 2005, in ASP Conf. Ser. 347, Astronomical Data Analysis Software and Systems XIV, ed. P. Shopbell, M. Britton, & R. Ebert (San Francisco, CA: ASP), 81

Maraston, C. 2005, MNRAS, 362, 799

Markevitch, M. 1998, ApJ, 504, 27

Markevitch, M. 2006, in The X-ray Universe 2005, ed. A. Wilson (ESA SP-617; Noordwijk: ESA), 723

Markevitch, M., Gonzalez, A. H., Clowe, D., et al. 2004, ApJ, 606, 819

Markevitch, M., Gonzalez, A. H., David, L., et al. 2002, ApJ, 567, L27

Marriage, T. A., Acquaviva, V., Ade, P. A. R., et al. 2011, ApJ, 737, 61

Mastropietro, C., & Burkert, A. 2008, MNRAS, 389, 967

Mauch, T., Murphy, T., Buttery, H. J., et al. 2003, MNRAS, 342, 1117

Maughan, B. J., Jones, L. R., Ebeling, H., & Scharf, C. 2004, MNRAS, 351, 1193

McNamara, B. R., O'Connell, R. W., & Sarazin, C. L. 1996, AJ, 112, 91

Mei, S., Holden, B. P., Blakeslee, J. P., et al. 2009, ApJ, 690, 42

Melin, J.-B., Bartlett, J. G., & Delabrouille, J. 2006, A&A, 459, 341

Menanteau, F., Ford, H. C., Motta, V., et al. 2006, AJ, 131, 208

Menanteau, F., González, J., Juin, J.-B., et al. 2010a, ApJ, 723, 1523

Menanteau, F., Hughes, J. P., Barrientos, L. F., et al. 2010b, ApJS, 191, 340

Menanteau, F., Hughes, J. P., Jimenez, R., et al. 2009, ApJ, 698, 1221

Merten, J., Coe, D., Dupke, R., et al. 2011, MNRAS, 417, 333

Mortonson, M. J., Hu, W., & Huterer, D. 2011, Phys. Rev. D, 83, 023015

Mullis, C. R., Rosati, P., Lamer, G., et al. 2005, ApJ, 623, L85

Navarro, J. F., Frenk, C. S., & White, S. D. M. 1997, ApJ, 490, 493

Nozawa, S., Itoh, N., & Kohyama, Y. 1998, ApJ, 508, 17

Peng, C. Y., Ho, L. C., Impey, C. D., & Rix, H.-W. 2010, AJ, 139, 2097

Poole, G. B., Babul, A., McCarthy, I. G., et al. 2007, MNRAS, 380, 437

Randall, S. W., Markevitch, M., Clowe, D., Gonzalez, A. H., & Bradač, M. 2008, ApJ, 679, 1173

Randall, S. W., Sarazin, C. L., & Ricker, P. M. 2002, ApJ, 577, 579

Ricker, P. M., & Sarazin, C. L. 2001, ApJ, 561, 621

Rosati, P., Tozzi, P., Ettori, S., et al. 2004, AJ, 127, 230

Rosati, P., Tozzi, P., Gobat, R., et al. 2009, A&A, 508, 583

Rottgering, H. J. A., Wieringa, M. H., Hunstead, R. W., & Ekers, R. D. 1997, MNRAS, 290, 577

Russell, H. R., Sanders, J. S., Fabian, A. C., et al. 2010, MNRAS, 406, 1721

Santos, J. S., Tozzi, P., Rosati, P., Nonino, M., & Giovannini, G. 2011, arXiv:1111.3642

Sehgal, N., Trac, H., Acquaviva, V., et al. 2011, ApJ, 732, 44

Sersic, J. L. 1968, Atlas de galaxies australes (Cordoba, Argentina: Observatorio Astronomico)

Shapley, A. E., Steidel, C. C., Erb, D. K., et al. 2005, ApJ, 626, 698

Sifón, C., Menanteau, F., Hasselfield, M., et al. 2012, arXiv:1201.0991

Stanford, S. A., Romer, A. K., Sabirli, K., et al. 2006, ApJ, 646, L13

Sunyaev, R. A., & Zeldovich, Y. B. 1972, Comments Astrophys. Space Phys., 4, 173

Swetz, D. S., Ade, P. A. R., Amiri, M., et al. 2011, ApJS, 194, 41

van Weeren, R. J., Brüggen, M., Röttgering, H. J. A., & Hoeft, M. 2011, MNRAS, 418, 230

Vikhlinin, A., Burenin, R. A., Ebeling, H., et al. 2009, ApJ, 692, 1033

Vikhlinin, A., van Speybroeck, L., Markevitch, M., Forman, W. R., & Grego, L. 2002, ApJ, 578, L107

Williamson, R., Benson, B. A., High, F. W., et al. 2011, ApJ, 738, 139

Yang, H.-Y. K., Bhattacharya, S., & Ricker, P. M. 2010, ApJ, 725, 1124